Check for updates

Earthquake Engineering & Structural Dynamics

WILEY

RESEARCH ARTICLE OPEN ACCESS

Rocking and Rolling of Rigid Polygons Under Seismic Excitation

Atif Rasheed | Christian Málaga-Chuquitaype

Department of Civil and Environmental Engineering, Imperial College London, London, UK

Correspondence: Christian Málaga-Chuquitaype (c.malaga@imperial.ac.uk)

Received: 4 March 2026 | **Revised:** 24 June 2026 | **Accepted:** 26 June 2026

Keywords: cyclic polygons | irregularity | pulse-like ground motion | rocking polygon | rolling polygon | seismic isolation

ABSTRACT

We present an event driven analytical framework for rigid cyclic polygons subjected to horizontal ground excitation in which uplift, impact, and successive pivot switching are treated within a unified non-smooth dynamical description. Rolling is defined as a sequence of energetically admissible transitions between neighbouring vertices tied to geometry, restitution, and excitation intensity. We demonstrate that the motion of a repetitive polygonal assembly layer can be reduced to a classical rocking equation with a modified frequency parameter governed by polygon geometry and superstructure-to-polygon mass ratio. By idealising rolling as a repeatable kinematic mechanism, response regimes are mapped as functions of polygon resolution and irregularity. Relevant response metrics are quantified, including cumulative maximum and cumulative permanent rotations, acceleration amplification, and energy dissipation. Increasing polygon resolution is found to promote bounded rolling-dominated regimes while reducing peak acceleration demands. When subjected to real earthquake records, more irregular polygons generally exhibit lower cumulative rotations across the range of intensities analysed, whereas peak accelerations remain strongly influenced by discrete impact events and by earthquake duration scaling. The proposed framework provides a preliminary rational basis for understanding rigid-body rocking-rolling isolation systems governed by geometry and contact kinematics.

1 | Introduction

The response of rigid bodies subjected to strong ground motion is a canonical example of non-smooth dynamics. Among these phenomena, rocking motion resulting from uplift and rotation about discrete contact points, which describes the seismic response of free-standing and partially restrained structures, has been extensively studied [1, 2]. Building on the analytical formulation derived by Housner [3], a large body of research has further examined rocking behaviour or rigid blocks using analytical [4, 5], numerical [6, 7], and experimental [8, 9] approaches, with particular emphasis on self-centring characteristics and energy dissipation through impacts. Within this prevailing framework, the coefficient of friction at the base is typically assumed to be sufficiently large to prevent sliding, such that the response is governed solely by uplift and rocking about discrete pivot points [10], while overturning is generally defined as the ultimate limit state associated with block instability [9, 11].

From a broader perspective, however, a rigid polygon of suitable geometry may, under an appropriate combination of ground-motion intensity and duration, undergo rolling motion through the successive activation of adjacent contact points. This behaviour can arise naturally once the rotation exceeds that of a single rocking cycle. This phenomenon has received little explicit attention in the scientific literature. Although related concepts involving the controlled migration of support contacts have been explored in engineered rocking systems, such as stepping frames [12] and rocking foundations [13, 14]; these studies differ

This is an open access article under the terms of the Creative Commons Attribution License, which permits use, distribution and reproduction in any medium, provided the original work is properly cited.
© 2026 The Author(s). *Earthquake Engineering & Structural Dynamics* published by John Wiley & Sons Ltd.

fundamentally in mechanics and intent, and do not directly address the behaviour of rolling rigid bodies.

Disregarding rolling to the adjacent pivot by terminating the response once the rotation exceeds a prescribed threshold is appropriate when overturning is the primary concern. However, rolling can be of interest for studying the response of certain seismic isolation systems [15–17] whose fundamental objective is to reduce the force transmission to the superstructure by allowing relative displacement at the base [18–20]. This objective can be achieved by exploiting geometry and contact kinematics [21] and cyclic polygons constitute the minimal tractable family for a first analytical study of these systems. Accordingly, our study can offer a first-order approximation to geometry-governed response mechanisms for certain isolation techniques, provided such rolling remains stable and does not lead to uncontrolled behaviour.

Despite this motivation, existing analytical frameworks face difficulties in representing transitions from rocking to rolling. Rolling requires systematic switching among multiple pivots at each transition which is generally absent from current rocking formulations. Moreover, for general polygonal or irregular geometries, the switching logic becomes asymmetric and cannot be captured reliably by a single stability threshold as derived for rectangular shapes. In addition, the distinction between controlled rolling and failure must be stated in analytical terms rather than inferred post hoc from numerical response histories. These limitations motivate the need for an event-based non-smooth framework that identifies transitions between neighbouring pivots, how energy is redistributed at impact, and how cumulative rotations leading to permanent translation emerges from the geometry under given excitation characteristics.

Rigid cyclic polygons (i.e., polygons with constant-radius circumcircle) provide a minimal and analytically tractable family of shapes within which these questions can be posed precisely in simple mathematical terms. Their vertices define a discrete set of candidate pivots, their resolution controls the spacing between successive pivots, and their geometry allows a clear transition from rocking to rolling. In addition, cyclic polygons form a natural bridge between the classical rectangular block and smoother rolling geometries, enabling a systematic study of how increasing geometric resolution alters admissibility of pivot transitions and the resulting balance between acceleration reduction and displacement accumulation [22–25].

In this paper, we develop an analytical formulation for the rocking and rolling response of rigid cyclic polygons subjected to horizontal ground excitation. Uplift initiation, impact, and pivot switching are treated as successive events within a unified event-driven framework grounded in non-smooth dynamics, allowing the governing equations to remain well defined across repeated impacts and contact transitions. Rolling is defined as a sequence of transitions between adjacent pivots, with admissibility criteria derived explicitly from energy and contact kinematics, thereby distinguishing stable rolling regimes without relying on ad hoc termination rules. Using this formulation, we characterise response regimes as functions of polygon resolution, polygon irregularity, and key dimensionless parameters that represent excitation intensity, frequency content relative to the rocking timescale, and impact energy dissipation. We then evaluate isolation-relevant response measures, including cumulative base displacement, peak accelerations, and energy dissipation. It should be noted that rigid-body rocking-rolling isolation systems of the type studied here are not currently recognised or permitted by major seismic design codes. The present work is therefore intended as an analytical baseline study of the underlying mechanics, providing the mechanistic understanding that must precede safety assessment, experimental validation, and eventual code consideration.

The remainder of the paper is organised as follows. Section 2 summarises the classical rocking formulation and establishes the notation, assumptions, and energetic quantities used throughout this paper. It presents the event-driven analytical framework for cyclic polygons and derives the equation of motion based on variational principles, including uplift conditions, impact laws, and admissibility criteria for pivot switching. Furthermore, an expression for the uplift threshold corresponding to isolation activation is also derived and discussed together with the energy dissipation at impact. Section 3 develops the geometric modelling of cyclic polygons with particular emphasis on their irregularity. It details the approach followed for obtaining the geometric characteristics of irregular cyclic polygons and their rolling responses. Section 4 presents a dimensional analysis and quantifies isolation-relevant performance metrics for regular and irregular polygonal geometries. Finally, Section 5 extends our findings to real earthquake responses by presenting a probabilistic evaluation of rigid cyclic polygons subjected to a set of real pulse-like ground motions.

2 | Analytical Framework

The analytical formulations available in the literature for rocking rigid bodies are inherently single-pivot, that is, they treat motion as governed by rotation about a single pivot point; and the allowable regime of motion is often limited by the slenderness angle. If this angle is exceeded during rocking, the solution is terminated and the response is classified as overturning. While such categorization is correct for rigid blocks not intended to roll, it prevents the analytical representation of rolling via repeated contact transitions. Such a chain of transitions is mechanically admissible for bodies with multiple potential support vertices. One such system was studied by Tsiatas et al. [14], who drew inspiration from Subbuteo, where multiple vertices can be in contact with the rigid support at different stages of the motion and hence provide a rolling isolation system. This system was, however, developed for the protection of uplifting bodies and does not allow for the successive rocking events leading to seismic isolation. Admittedly, rolling-type motion and its accumulation of lateral relative displacement cannot be explained within classical rocking frameworks.

2.1 | Background and Modelling Assumptions

The analytical framework proposed herein to study the dynamics of rigid cyclic polygons, shares some foundational assumptions with the classical formulations for rocking dynamics. More precisely, the use of a single rotational degree of freedom, the definition of uplift thresholds based on geometry, and accounting

10969845, 2026, 12, Downloaded from https://onlinelibrary.wiley.com/doi/10.1002/eqe.70244 by Imperial College London, Wiley Online Library on [12/10/2026]. See the Terms and Conditions (https://onlinelibrary.wiley.com/terms-and-conditions) on Wiley Online Library for rules of use; OA articles are governed by the applicable Creative Commons License

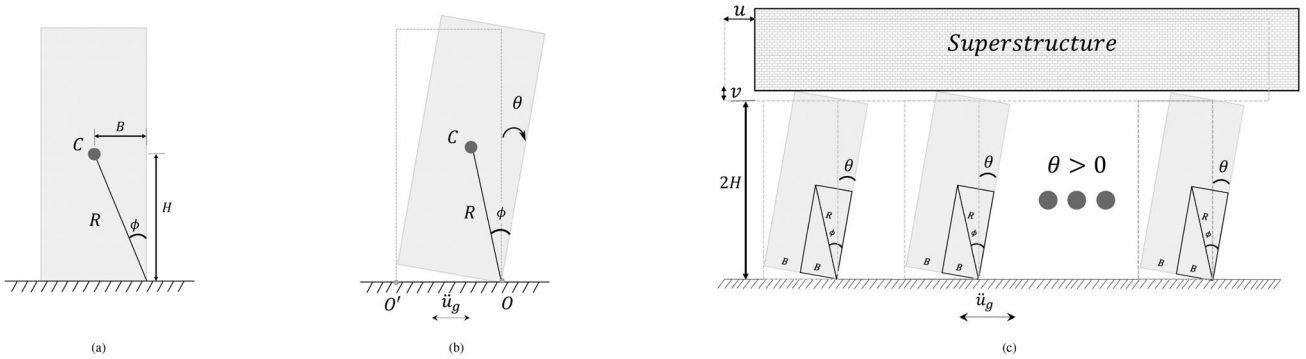


FIGURE 1 | Rocking behaviour of a rigid block and frame system: (a) Rectangular block at rest, (b) Rectangular block during rocking motion, and (c) Rocking frame.

for the energy lost during impact by means of a coefficient of restitution, are all classical assumptions also adopted in this work. Accordingly, Housner's original rocking model, which embodies these core principles, provides the natural starting point for building our new, more general rolling dynamics framework. In Housner's model, the rotation, denoted by θ as shown in Figure 1, is taken as the sole degree of freedom. Besides, the assumption of sufficiently large friction eliminates the possibility of sliding. Therefore, rocking is initiated when the overturning moment due to inertial forces about the pivot point exceeds the restoring moment provided by the block's weight. This condition can be expressed as:

$$\left|\ddot{u}_g\right| \geq g\tan(\phi) \tag{1}$$

where g is the acceleration due to gravity and ϕ is the slenderness ratio of the block. Notably, the dynamics of such a system can be characterized by the frequency parameter $p = \sqrt{\frac{3g}{4R}}$. In this case, the mass moment of inertia (MMI) about one of the rocking vertices is $I_0 = \frac{4}{3}mR^2$, where m is the mass of the block and R is the distance from the rocking vertex to the centroid C (see Figure 1).

The equations of motion for rocking about the left or right pivot of a rigid block subjected to horizontal ground acceleration are directionally distinct and have been derived in several studies [2, 10, 26]. They can be written in the following compact form:

$$\ddot{\theta}(t) = -p^2\left(\sin[\phi\,\mathrm{sgn}(\theta(t)) - \theta(t)] + \frac{\ddot{u}_g}{g}\cos[\phi\,\mathrm{sgn}(\theta(t)) - \theta(t)]\right) \tag{2}$$

This model was later extended by Makris et al. [1] to systems consisting of multiple free-standing rectangular columns supporting a rigid beam, representing a frame (see Figure 1). They reached two significant conclusions: (a) the dynamics of such frames are governed by rocking, which acts as the fundamental mechanism for seismic energy dissipation, and (b) the uplift during rocking is independent of the mass of either the epistyle or the frieze above. An empirical expression for the dynamics of such frame systems was also derived:

$$\ddot{\theta} = -\frac{1+2\gamma}{1+3\gamma}p^2\left(\sin[\alpha\,\mathrm{sgn}(\theta(t)) - \theta(t)] + \frac{\ddot{u}_g(t)}{g}\cos[\alpha\,\mathrm{sgn}(\theta(t)) - \theta(t)]\right) \tag{3}$$

Equation (3) is structurally identical to Equation (2), except for the modification of the frequency parameter. In this latter case, p^2 is scaled by the factor $\frac{1+2\gamma}{1+3\gamma}$, where γ denotes the ratio of the mass of the superimposed beam (or frieze) to the mass of the free-standing columns.

Building upon these classical rocking formulations, we now consider the ideal case of an isolation layer composed of a set of rigid cyclic polygons supporting a rigid superstructure (see Figure 2). Unlike rectangular blocks, cyclic polygons possess multiple vertices that may act as pivots if excited horizontally. Like conventional rocking blocks, cyclic polygons exhibit uplift once the ground excitation exceeds a threshold acceleration (as derived in Section 2.3). The geometry of cyclic polygons, therefore, provides a natural conceptual transition between rocking and rolling. As the resolution (i.e., number of sides) of a cyclic polygon increases, its geometrical properties asymptotically approach those of a circle, while its motion remains governed by discrete contact mechanics. In this sense, cyclic polygons provide a bridge between classical rocking block dynamics and idealized rolling bodies while requiring a fundamentally revised stability framework: transition to the adjacent pivot is no longer interpreted as failure, but is instead treated as an admissible event within the sequence of contact transitions conforming the rolling response, as dictated by geometry and energy balance. A variational formulation is used below to derive the governing equations of motion of such a system.

2.2 | Dynamics of Cyclic Polygons

An idealized model that captures the fundamental mechanics of a single-degree-of-freedom cyclic polygon is shown in Figure 3. For the sake of simplicity, a regular polygon with n equal sides is assumed (polygon irregularity is introduced in Section 3). This allows a straightforward geometric representation within a circumscribed circle of radius r_c, which is equal to the distance from the centroid to any vertex. Rocking motion is anticipated to occur about the base contact points L and R (Figure 3), while if the ground motion is strong enough, the cyclic block may roll onto neighbouring vertices on either side. Our analysis assumes, as customary, a sufficiently large friction coefficient to prevent sliding during horizontal ground excitation, and uplift, rocking, and rolling to the

10969845, 2026, 12, Downloaded from https://onlinelibrary.wiley.com/doi/10.1002/eqe.70244 by Imperial College London, Wiley Online Library on [12/10/2026]. See the Terms and Conditions (https://onlinelibrary.wiley.com/terms-and-conditions) on Wiley Online Library for rules of use; OA articles are governed by the applicable Creative Commons License

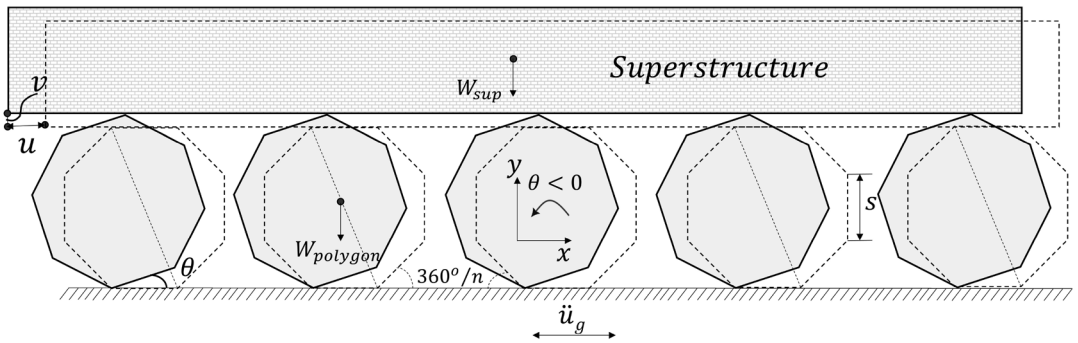
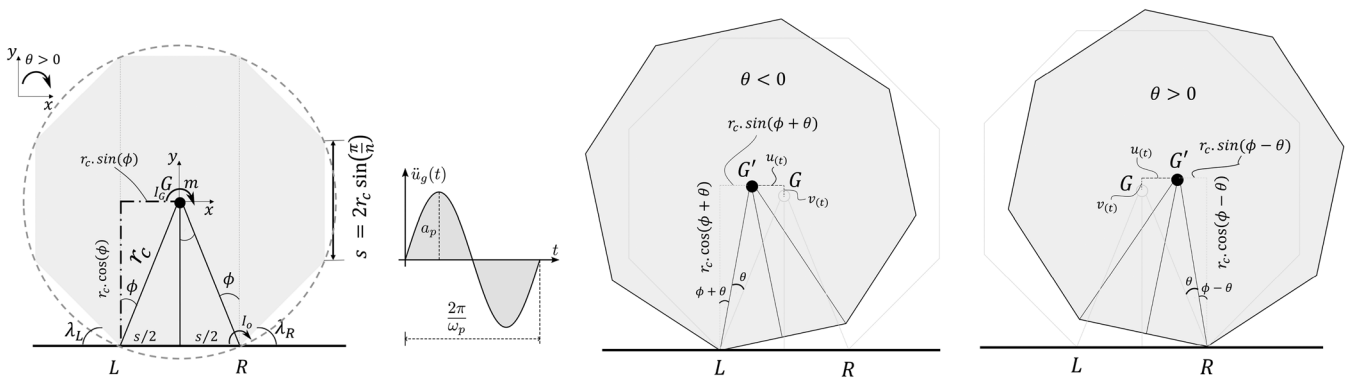


FIGURE 2 | Idealized layer of N rigid cyclic polygons sustaining a rigid superstructure of weight W_{sup} subjected to horizontal ground acceleration $\ddot{u}_g$.



(a) Initial position of the cyclic polygon. (b) An idealized sine pulse. (c) Rocking anti-clockwise due to rightward ground movement. (d) Orientation after rocking to the left.

FIGURE 3 | Different stages of motion of a generalized single cyclic polygon under horizontal ground acceleration, $\ddot{u}_g$, in the form of a sinusoidal pulse of amplitude a_p and frequency ω_p.

adjacent contact points are considered as the primary modes of motion.

The overlying rigid superstructure (load-bearing mass), shown schematically in Figure 2, influences the system response and is characterized by its mass m_{sup}. Prior to uplift, the cyclic polygons behave as perfectly rigid elements with infinite stiffness. Once rocking initiates, stiffness decreases as the rotation angle θ increases, reaching a maximum rotation of λ_R or λ_L. At this threshold, a new pivot point is engaged, enabling the cyclic polygons either to rock or to roll forward or backward until another pivot point becomes engaged or the block comes to rest.

The kinematics of a generalized system are described by the horizontal displacement $u(t)$ and vertical uplift $v(t)$, both of which depend on the rotation angle $\theta(t)$ about the pivot points L and R (Figure 3). The total kinetic energy (T) of the system, defined as the sum of the rotational kinetic energy of the cyclic polygons and the translational kinetic energy of the superstructure, remains the same for rightward ($\theta(t) > 0$) and leftward ($\theta(t) < 0$) rocking:

$$T = \frac{1}{2} I_o (\dot{\theta})^2 + \frac{1}{2} m_{\text{sup}} \left(\dot{u}^2 + \dot{v}^2 \right) \tag{4}$$

where I_o is the moment of inertia of the cyclic polygon about the pivot point, and $\dot{\theta}$ is the angular velocity, $\dot{u}$ and $\dot{v}$ are the rectangular components of the velocity which are obtained by differentiating the kinematic expressions of the centroid displacements, $u(t)$ and $v(t)$. These displacements are shown in Figure 3c assuming leftward rocking motion (numerically identical to rightward rocking, but with θ of the opposite sign).

Since Equation (4) represents the kinetic energy of the system when there is one cyclic polygon, generalising for N polygons we obtain:

$$T = N \frac{1}{2} I_O (\dot{\theta})^2 + \frac{1}{2} m_{sup} \left(\dot{u}^2 + \dot{v}^2 \right) \tag{5}$$

Or, substituting the values of $\dot{u}$ and $\dot{v}$ and simplifying:

$$T = \frac{1}{2} \left(N I_o + m_{\text{sup}} r_c^2 \right) (\dot{\theta})^2 \tag{6}$$

The Lagrangian of the system is defined as:

$$\mathcal{L} = T - V \tag{7}$$

where T and V denote the kinetic and potential energies of the system, respectively. And the corresponding Euler–Lagrange equation is expressed as:

$$\frac{d}{dt} \left(\frac{\partial \mathcal{L}}{\partial \dot{q}} \right) - \frac{\partial \mathcal{L}}{\partial q} = Q \tag{8}$$

10969845, 2026, 12, Downloaded from https://onlinelibrary.wiley.com/doi/10.1002/eqe.70244 by Imperial College London, Wiley Online Library on [12/10/2026]. See the Terms and Conditions (https://onlinelibrary.wiley.com/terms-and-conditions) on Wiley Online Library for rules of use; OA articles are governed by the applicable Creative Commons License

Here, q represents the generalised coordinate, and Q the generalised force. In this analysis, the generalized coordinate is the rotation angle θ, which will be used in place of q in the subsequent equations.

Employing the Principle of Virtual Work to determine the generalized force Q for a system subjected to external forces $\mathbf{F}_i$ and corresponding virtual displacements $\delta\mathbf{r}_i$, we obtain:

$$\sum_i \mathbf{F}_i \cdot \left(\frac{\partial \mathbf{r}_i}{\partial\theta}\delta\theta\right) = \left(\sum_i \mathbf{F}_i \cdot \frac{\partial \mathbf{r}_i}{\partial\theta}\right)\delta\theta = 0 \tag{9}$$

Thus, we define the generalized force as:

$$Q = \sum_i \mathbf{F}_i \cdot \frac{\partial \mathbf{r}_i}{\partial\theta} \tag{10}$$

which is the total virtual work δW done by the external forces per unit virtual displacement in θ, that is,

$$Q = \frac{\delta W}{\delta\theta} \tag{11}$$

In our system, two external forces are present: the inertial force due to horizontal ground acceleration and the gravitational force due to weight. The inertial (horizontal) force is given by

$$F_{\text{inertia}} = -(m_{\text{sup}} + NM_{\text{polygon}})\ddot{u}_g,$$

and its associated virtual displacement is δu. On the other hand, the gravitational force is

$$W = -(m_{\text{sup}} + NM_{\text{polygon}})g$$

acting vertically downward, with associated virtual displacement δv.

Under horizontal ground acceleration $\ddot{u}_g$, two scenarios arise based on the sign of $\theta(t)$:

Case 1: Rocking to the left ($\theta(t) < 0$)

In this case, the virtual rotation is counter-clockwise. Consequently, $\delta u < 0$ and $\delta v > 0$. The total virtual work is given by:

$$\begin{aligned}\delta W = &\left[-(m_{\text{sup}} + NM_{\text{polygon}})\ddot{u}_g\right](-\delta u)\\ &+ \left[-(m_{\text{sup}} + NM_{\text{polygon}})g\right](+\delta v)\end{aligned}$$

$$\delta W = (m_{\text{sup}} + NM_{\text{polygon}})\ddot{u}_g\delta u - (m_{\text{sup}} + NM_{\text{polygon}})g\delta v \tag{12}$$

or, in simplified form:

$$\delta W = (m_{\text{sup}} + NM_{\text{polygon}})\left(\ddot{u}_g\delta u - g\delta v\right) \tag{13}$$

Considering that:

$$\delta u = \frac{\partial u}{\partial\theta}\delta\theta \qquad \delta v = \frac{\partial v}{\partial\theta}\delta\theta \tag{14}$$

we obtain:

$$\delta W = (m_{\text{sup}} + NM_{\text{polygon}})\left(\ddot{u}_g\frac{du}{d\theta} - g\frac{dv}{d\theta}\right)\delta\theta$$

Therefore, the generalized force becomes:

$$Q = \frac{\delta W}{\delta\theta} = (m_{\text{sup}} + NM_{\text{polygon}})\left(\ddot{u}_g\frac{du}{d\theta} - g\frac{dv}{d\theta}\right) \tag{15}$$

which can be simplified to:

$$Q_{\theta^-} = r_c(m_{\text{sup}} + NM_{\text{polygon}})\left(\ddot{u}_g\cos(\phi - \theta) - g\sin(\phi - \theta)\right) \tag{16}$$

Case 2: Rocking to the Right ($\theta(t) > 0$)

For clockwise virtual rotation, both $\delta u > 0$ and $\delta v > 0$. The corresponding virtual work becomes:

$$\begin{aligned}\delta W = &\left[-(m_{\text{sup}} + NM_{\text{polygon}})\ddot{u}_g\right](+\delta u)\\ &+ \left[-(m_{\text{sup}} + NM_{\text{polygon}})g\right](+\delta v)\end{aligned}$$

$$\delta W = -(m_{\text{sup}} + NM_{\text{polygon}})\ddot{u}_g\delta u - (m_{\text{sup}} + NM_{\text{polygon}})g\delta v \tag{17}$$

Substituting the virtual displacements, we have:

$$\delta W = -(m_{\text{sup}} + NM_{\text{polygon}})\left(\ddot{u}_g\frac{du}{d\theta} + g\frac{dv}{d\theta}\right)\delta\theta$$

yielding the generalized force as:

$$Q = \frac{\delta W}{\delta\theta} = -(m_{\text{sup}} + NM_{\text{polygon}})\left(\ddot{u}_g\frac{du}{d\theta} + g\frac{dv}{d\theta}\right) \tag{18}$$

which can be simplified to:

$$Q_{\theta^+} = r_c(m_{\text{sup}} + NM_{\text{polygon}})\left(\ddot{u}_g\cos(\phi + \theta) + g\sin(\phi + \theta)\right) \tag{19}$$

Having generalized forces for both cases, we simplify the Euler-Lagrange (Equation 8) by substituting Equation (7) into Equation (8), arriving at:

$$\frac{d}{dt}\left(\frac{\partial T}{\partial\dot{\theta}}\right) - \frac{d}{dt}\left(\frac{\partial V}{\partial\dot{\theta}}\right) - \frac{\partial T}{\partial\theta} + \frac{\partial V}{\partial\theta} = Q \tag{20}$$

The potential energy of the system is independent of the rotational angle θ, so the Equation (20) reduces to,

$$\frac{d}{dt}\left(\frac{\partial T}{\partial\dot{\theta}}\right) - \frac{\partial T}{\partial\theta} = Q \tag{21}$$

Substituting the expression for the kinetic energy of the system (Equation 6) into Equation (21), and realizing that the expression of T in Equation (6) is not a function of θ, thus $\frac{\partial T}{\partial\theta}$ becomes zero, and we are left with:

$$\frac{d}{dt}\left(\frac{\partial\left[\frac{1}{2}\left(NI_o + m_{\text{sup}}r_c^2\right)(\dot{\theta})^2\right]}{\partial\dot{\theta}}\right) - 0 = Q \tag{22}$$

Evaluating the above equation, we get:

$$(NI_o + m_{\text{sup}}r_c^2)\ddot{\theta} = Q \tag{23}$$

10969845, 2026, 12, Downloaded from https://onlinelibrary.wiley.com/doi/10.1002/eqe.70244 by Imperial College London, Wiley Online Library on [12/10/2026]. See the Terms and Conditions (https://onlinelibrary.wiley.com/terms-and-conditions) on Wiley Online Library for rules of use; OA articles are governed by the applicable Creative Commons License

By substituting the corresponding generalized force expressions (Equations 16 and 19) into Equation (23), the respective equations of motion are obtained for the two cases, namely $\theta_t < 0$ and $\theta_t > 0$. Finally, combining these results provides a comprehensive equation capable of describing the complete motion of the system under ground excitation:

$$\ddot{\theta} = -p^2\left(\sin(\phi\,\mathrm{sgn}(\theta_t) - \theta_t) + \frac{\ddot{u}_g}{g}\cos(\phi\,\mathrm{sgn}(\theta_t) + \theta_t)\right) \tag{24}$$

with:

$$p = \sqrt{\frac{g \cdot r_c(\gamma+1)}{\frac{I_o}{M_{polygon}} + \gamma \cdot r_c^2}} \tag{25}$$

where p is the frequency parameter, $\gamma = \frac{m_{\mathrm{sup}}}{N.M_{\mathrm{polygon}}}$ is the ratio of the superstructure mass, m_{sup}, to the mass of all the N cyclic polygons.

For a regular cyclic polygon, the MMI about any vertex is given by $I_o = r_c^2 \cdot M_{polygon}\left[\frac{7+2\cos^2\left(\frac{\pi}{n}\right)}{6}\right]$ (see Appendix A). Let us substitute $X = \frac{7+2\cos^2\left(\frac{\pi}{n}\right)}{6}$ so the equation for the MMI becomes $I_o = r_c^2 \cdot M_{polygon} \cdot X$ with which the frequency parameter (Equation 25) reduces to:

$$p = \sqrt{\frac{g(\gamma+1)}{r_c(X+\gamma)}} \tag{26}$$

In principle, Equations (25) and (26) are equivalent; however, Equation (25) can be employed in cases involving an irregular cyclic polygon for which the MMI cannot be determined straightforwardly from geometric considerations. In such cases, the two-dimensional divergence theorem, as explained in Section 3, can be applied. Conversely, Equation (26) is used when dealing with a regular polygon of known geometry.

Equation (24) is sufficiently general to capture the motion associated with any type of cyclic polygon. A numerical procedure is developed in MATLAB [27] to integrate this nonlinear differential equation using its `ode45` solver and employed to generate the results underpinning the discussions in the following sections.

2.3 | Initiation Threshold for Uplift of the Cyclic Polygon System

During a permissible virtual rotation, denoted by $\delta\theta$ and illustrated in Figure 2, the application of the Principle of Virtual Work yields:

$$(m_{\mathrm{sup}}\ddot{u}_g)\delta u + (NM_{\mathrm{polygon}}\ddot{u}_g)\delta u - (m_{\mathrm{sup}}g)\delta v - (NM_{\mathrm{polygon}}g)\delta v = 0$$

This expression can be rearranged as:

$$\begin{aligned}&(m_{\mathrm{sup}}\ddot{u}_g)\,\delta u + (NM_{\mathrm{polygon}}\ddot{u}_g)\,r_c\cos\phi\,\delta\theta\\ &= (m_{\mathrm{sup}}g)\,\delta v + (NM_{\mathrm{polygon}}g)\,r_c\sin\phi\,\delta\theta\end{aligned} \tag{27}$$

Since uplift may occur in either direction, the general form of this expression remains unchanged. Without loss of generality, the system is assumed to be on the verge of counterclockwise rocking ($\theta < 0$) and the corresponding virtual displacements are:

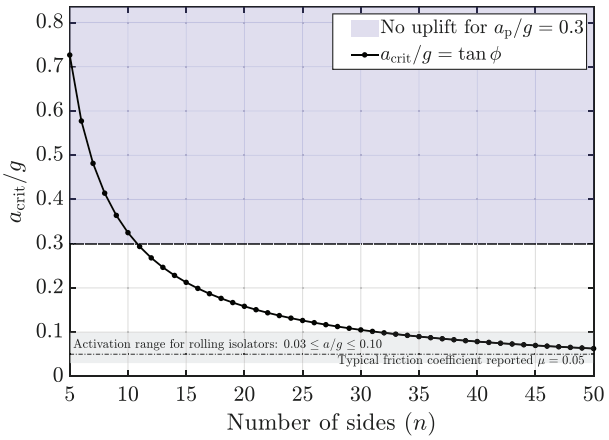


FIGURE 4 | Geometry-governed uplift activation threshold for regular cyclic polygons subjected to a sine pulse base excitation. The blue shaded region denotes the no-uplift activation domain for the case of a sine pulse of amplitude $a_p/g = 0.3$, as an example. The grey band shows activation thresholds for various available isolators. Note that the mechanics of these deformable isolators and the rigid polygons studied here are different and their activation levels are indicated for contextual reference only.

$$\delta u = r_c\cos(\phi - \theta)\,\delta\theta \tag{28}$$

$$\delta v = r_c\sin(\phi - \theta)\,\delta\theta \tag{29}$$

Substituting Equations (28) and (29) into Equation (27) leads to:

$$\begin{aligned}&(m_{\mathrm{sup}}\ddot{u}_g)\cos(\phi-\theta) + (NM_{\mathrm{polygon}}\ddot{u}_g)\cos\phi\\ &= (m_{\mathrm{sup}})\sin(\phi-\theta) + (NM_{\mathrm{polygon}})g\sin\phi\end{aligned} \tag{30}$$

Since the threshold for uplift corresponds to the onset of rocking, the system is initially at $\theta = 0$. At this rocking-initiation stage the ground acceleration is denoted by a_{crit}, representing the uplift threshold. Therefore,

$$(m_{\mathrm{sup}} + NM_{\mathrm{polygon}})\,a_{crit}\cos\phi = (m_{\mathrm{sup}}g + NM_{\mathrm{polygon}}g)\,\sin\phi \tag{31}$$

and solving for a_{crit} yields the uplift threshold acceleration

$$a_{crit} = g\tan\phi \tag{32}$$

which has the same form as available equations for uplift threshold in rocking blocks [2] but is now expressed in terms of the corner angle (ϕ) of the cyclic polygon. This confirms that the susceptibility of a cyclic polygon to uplift is governed by its geometry rather than its weight. Cyclic polygons with larger corner angles or fewer number of sides will require, in general, higher accelerations to initiate rocking, whereas shapes approaching circularity exhibit considerably lower uplift thresholds. The response of rigid polygons to sinusoidal pulses of different amplitudes, a_p, and frequencies ω_p is presented in Figures 4 and 5.

10969845, 2026, 12, Downloaded from https://onlinelibrary.wiley.com/doi/10.1002/eqe.70244 by Imperial College London, Wiley Online Library on [12/10/2026]. See the Terms and Conditions (https://onlinelibrary.wiley.com/terms-and-conditions) on Wiley Online Library for rules of use; OA articles are governed by the applicable Creative Commons License

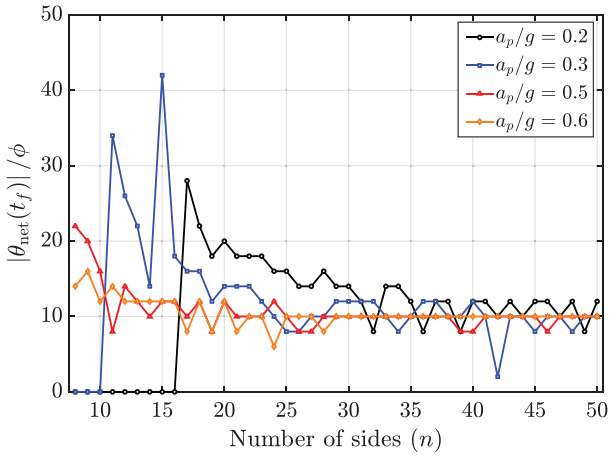


FIGURE 5 | Final permanent (residual) cumulative rotation, $|\theta_{\text{net}}(t_f)|/\phi$, of cyclic polygons under a horizontal base sinusoidal pulse of different amplitudes, a_p/g, and constant pulse frequency, $\omega_p = 1$ rad/s. The threshold intensity for uplift initiation is lower for cyclic polygons with smaller corner angles ϕ or more sides. An asymptotic minimum cumulative rotation is observed for all excitation intensities as the number of sides increases.

Figure 4 illustrates the evolution of a_{crit} as a function of n for regular cyclic polygons of fixed circumscribed radius r_c, showing that shapes approaching circularity activate at substantially smaller acceleration ratios. This geometric dependence highlights the importance of selecting cyclic polygons shapes with carefully tuned corner angles (ϕ) to achieve the desired activation level if used as part of an isolation layer. For example, if a sinusoidal pulse of amplitude $a_p/g = 0.30$ is expected, the blue shaded area in Figure 4 will denote no-uplift activation, indicating that for this particular ground-motion intensity, a polygon of at least 11 sides will be needed to activate uplift. To place the predicted uplift thresholds within the broader isolation context, Figure 4 also shows representative acceleration ratios associated with gravity-based isolation mechanisms governed by friction. For instance, the poly-tetrafluoroethylene (PTFE, commonly known as Teflon) sliding bearings activate once the inertial demand exceeds the frictional resistance. This leads to characteristic activation acceleration ratios, for pure rolling isolators, depending on velocity, pressure and contact conditions, typically reported in the approximate range $0.03 \leq a/g \leq 0.10$ [28–33]. It should be stressed that the mechanics of these deformable isolators differ substantially from those of the rigid polygons studied here and their activation levels are indicated for contextual reference only.

The ground acceleration associated with the initiation of rolling in a cylindrical body with a friction coefficient of $\mu = a/g \approx 0.05$ [34] is also shown in Figure 4 as an asymptotic limit. Nonetheless, for an ideal cyclic polygon, as $n \to \infty$, the corner angle tends to zero, $\phi \to 0$. Consequently, the uplift threshold also tends to zero, $a_{crit}/g \to 0$, which constitutes the limiting case of an ideally rigid circular body on a flat surface, neglecting local indentations and contact friction.

Figure 5 presents the final (permanent) cumulative rotations, $|\theta_{\text{net}}(t_f)|/\phi$, or residual rotation at the end of the motion (i.e., at time t_f) of cyclic polygons with different numbers of sides and fixed circumscribed radius, r_c, subjected to base sinusoidal pulses of different amplitudes, a_p/g and constant frequency, $\omega_p = 1$ rad/s. The clear dependence of a_{crit} on the polygonal geometry mentioned before is also clearly seen in this figure. Ground motions of lower a_p/g values will only induce motion of polygons with a correspondingly higher number of sides, that is, a null cumulative rotation is observed for polygons of $n \leq 10$ under a ground-motion of $a_p/g = 0.3$ while at least $n = 17$ sides are needed to start accumulating rotations when $a_p/g = 0.2$. Interestingly, as the number of sides increases, the final cumulative rotations tend to stabilize around a value of $|\theta_{\text{net}}(t_f)|/\phi \approx 10$ in Figure 5. This highlights the importance of the duration of the ground-motion, as further illustrated in Figure 6 where the rotation histories of polygons of various numbers of sides under sinusoidal pulses of different frequencies are reported. Figure 6 shows that the final permanent cumulative rotation, $|\theta_{\text{net}}(t_f)|/\phi$, of polygons with more sides ($n \geq 21$) tend to coalesce around a single value and that this value gets smaller with higher ground-motion frequencies (i.e., shorter pulse durations). This implies that the energetic length of the ground-motion [35, 36] plays a key role in the response of rolling systems.

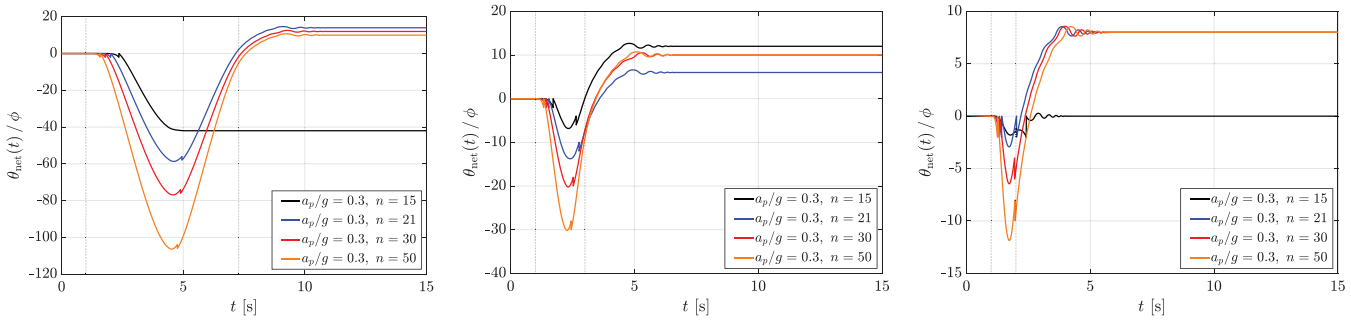
2.4 | Energy Dissipation and Impact

As noted previously, the governing equation of motion (Equation 24) and the uplift condition (Equation 32) derived above define a non-smooth, event-driven dynamical system that cannot be solved in closed form. Therefore, numerical integration is used to evaluate the response to ground excitations via MATLAB [27] `ode45` solver. This simulation is based on an event screening algorithm that identifies different phases and transition stages like initialization of uplift, continuous rotation, impacts or pivot transitions. During each continuous phase, the equation of motion is integrated until an event condition is satisfied. The angular velocity is updated after each impact based on Equation (33). Following earlier studies by Augusti and Sinopoli [37], Prieto et al. [38], and Yilmaz et al. [39], impact is modelled through the introduction of a coefficient of restitution that relates the angular velocity immediately after impact, $\dot{\theta}^+$, to that immediately prior to impact, $\dot{\theta}^-$:

$$\dot{\theta}^+ = \nu\dot{\theta}^- \tag{33}$$

Hence, energy dissipation in the system is assumed to occur exclusively through impact events. Two distinct impact configurations are considered. The first is a landing and reversal impact. This occurs when the body returns towards the symmetric configuration, $\theta = 0$, after a rocking motion that does not induce pivot switching. The second configuration is a rolling transition impact. This occurs when the rotation reaches the rolling threshold on either side, that is, $\theta = \lambda_R$ or $\theta = -\lambda_L$ as shown in Figure 3a. This event activates a new pivot and defines a new base edge for the subsequent motion. In both cases, the velocities of the supported mass are kinematically related to the angular velocity, $\dot{\theta}$. As a result, the restitution update corresponds to an instantaneous reduction in the total kinetic energy of the system. An expression for restitution of rigid rectangular blocks was proposed by Housner based on conservation of angular momentum implying that this coefficient depends on the slenderness ratio of the block. It is now well established that the

10969845, 2026, 12, Downloaded from https://onlinelibrary.wiley.com/doi/10.1002/eqe.70244 by Imperial College London, Wiley Online Library on [12/10/2026]. See the Terms and Conditions (https://onlinelibrary.wiley.com/terms-and-conditions) on Wiley Online Library for rules of use; OA articles are governed by the applicable Creative Commons License



(a) $\omega_p = 1$ rad/s. (b) $\omega_p = \pi$ rad/s. (c) $\omega_p = 2\pi$ rad/s.

FIGURE 6 | Rotational response histories of polygons with different numbers of sides subjected to sinusoidal pulses of constant amplitude and varying frequency. The final cumulative rotation of polygons with a larger number of sides tends to converge toward a single value, which decreases as the frequency of the ground-motion increases.

coefficient of restitution is influenced by factors beyond geometry alone, including contact conditions, frictional characteristics, and material properties [40–43]. However, incorporating such dependencies would require a more detailed contact mechanics formulation, which is beyond the scope of the current study. Hence, in this paper, the coefficient of restitution is treated as an independent parameter, consistent with the approach adopted by Hogan [26] and supported by experimental observations [44–46]. The restitution coefficient values used throughout this study, $\nu = 0.85$ to 0.95, cover a range representative of stone–stone and concrete–concrete contact types previously used in the literature [47, 48].

Within this formulation, the energy dissipated at the k-th impact is quantified as the reduction in total kinetic energy across the instantaneous velocity update. This quantity is defined as the difference between the kinetic energy immediately before impact and that immediately after impact, namely $\Delta E_k = T_k^- - T_k^+$. This definition captures the energy loss associated with impact. For a system composed of an array of N polygons rocking in phase beneath a rigid superstructure (like in Figure 2), the total kinetic energy is expressed in terms of the angular velocity, $\dot{\theta}$. The contribution of each polygon is represented through its moment of inertia, I_o, and the radius of its centre of mass, r_c. The contribution of the supported superstructure mass is represented through its mass, m_{sup}. Under these assumptions, the total kinetic energy of the system is given by Equation (6). Thus, the energy dissipated at the k-th impact can be written explicitly in terms of the angular velocity before and after impact. The resulting expression is:

$$\Delta E_k = \frac{1}{2}\left(N I_o + m_{\text{sup}} r_c^2\right)\left[(\dot{\theta}_k^-)^2 - (\dot{\theta}_k^+)^2\right] \tag{34}$$

The cumulative dissipated energy is then obtained by summing the energy losses over all impact defined as $E_{\text{diss}}(t) = \sum_{t_k \le t} \Delta E_k$. The resulting energy history is, therefore, stepwise in time as shown in Figure 6c.

To enable comparison across different polygon resolutions and system configurations, the cumulative dissipated energy is expressed in normalized form. The normalization is performed using a characteristic gravitational energy scale defined as:

$$E_{\text{ref}} = (N m_{\text{poly}} + m_{\text{sup}})\, g\, r_c \tag{35}$$

here, $N m_{\text{poly}} + m_{\text{sup}}$ represents the total rocking mass of the capped array, while r_c denotes a characteristic geometric length measured from the active pivot to the centroid. This reference quantity has dimensions of energy and represents the order of magnitude of the gravitational potential energy associated with lifting the system through a displacement comparable to its geometric scale. Since gravity provides the restoring mechanism governing rocking motion [2, 3], this energy scale constitutes a physically meaningful reference consistent with established similarity principles in rocking dynamics [42]. Using this normalization, a dimensionless measure of dissipated energy is obtained as:

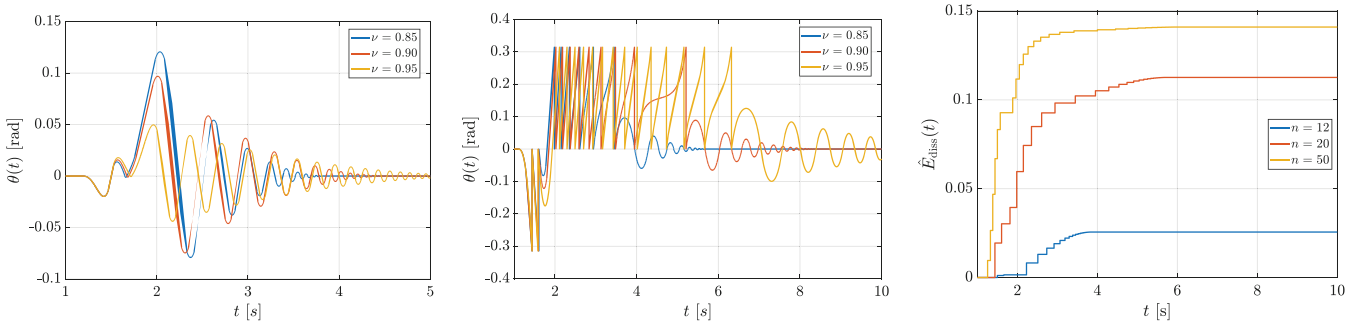
$$\hat{E}_{\text{diss}}(t) = \frac{E_{\text{diss}}(t)}{E_{\text{ref}}} \tag{36}$$

this representation enables a direct comparison of dissipation histories across different values of n while removing bias associated with absolute mass or geometric scaling.

To clarify the mechanical implications of the adopted restitution law, Figure 7 illustrates the effect of the coefficient of restitution on the rotational response and on the cumulative dissipated energy. The rotation histories in Figure 6a,b show that the coefficient of restitution does not influence the uplift condition nor modifies the governing equation during continuous rocking. Its role is restricted to impact events. As the restitution coefficient decreases, the amplitude of successive rocking cycles decays more rapidly. The geometric dependence of this mechanism becomes further evident when comparing different polygons. For $n = 12$, rocking excursions are relatively large, as shown in Figure 6a, along with longer time intervals between consecutive impacts. This leads to sharp reductions in rotation response. On the other hand, for $n = 20$, the excursions are smaller due to frequent impacts, which lead to lower energy loss per event. The cumulative effect is a smoother and more gradual motion decay. This comparison shows that polygon resolution governs not only uplift characteristics, but also the temporal distribution of dissipative events.

The dissipation curves shown in Figure 6c demonstrate that for lower n, the steps are fewer but larger, reflecting higher angular velocities at impact. For larger n, the energy increases through many smaller increments, indicating more frequent but

10969845, 2026, 12, Downloaded from https://onlinelibrary.wiley.com/doi/10.1002/eqe.70244 by Imperial College London, Wiley Online Library on [12/10/2026]. See the Terms and Conditions (https://onlinelibrary.wiley.com/terms-and-conditions) on Wiley Online Library for rules of use; OA articles are governed by the applicable Creative Commons License



(a) Regular polygon with $n = 12$.

(b) Regular polygon with $n = 20$.

(c) Cumulative normalized energy dissipation.

FIGURE 7 | Influence of the coefficient of restitution on the local rocking response and cumulative dissipated energy under a sine pulse with $a_p = 0.3g$ and $\omega_p = 2\pi$ rad/s. Panels (a) and (b) show the local rocking rotation histories $\theta(t)$ for regular polygons with $n = 12$ and $n = 20$, respectively, for different values of ν. Panel (c) presents the normalized cumulative dissipated energy $\hat{E}_{\text{diss}}(t)$ for $n = 12$, 20, and 50 at fixed $\nu = 0.85$. The stepwise increase in $\hat{E}_{\text{diss}}(t)$ reflects the assumption that energy dissipation occurs only at discrete impact events.

less energetic pivot transitions. The total dissipated energy at the end of motion remains strongly dependent on both geometry and restitution parameter. These observations highlight two central features of the proposed framework. First, the dissipation mechanism is mechanically transparent and fully event-based. Second, polygon geometry controls how this dissipation is distributed in time. Highly faceted polygons distribute dissipation over many small impacts, while low sided geometries dissipate energy in fewer but more energetic events. Figure 7 presents a direct confirmation that increased geometric resolution enhances dissipation capacity through controlled rolling transitions.

3 | Irregularity in Cyclic Polygons

This section presents and discusses the modifications required to model complex irregular shapes subjected to rolling motion caused by earthquakes. Such irregular shapes can represent, for example, stone blocks used in indigenous low-cost isolation systems of the type studied in [17]. For cyclic regular polygons, the centroid, area, and moment of inertia are calculated directly using well-defined geometric relations. For irregular cyclic polygons, however, the two dimensional divergence theorem (Green's theorem [49]) is employed to compute the area and MMI. In addition, the procedure for the generation of consistent irregular cyclic polygons is non-trivial and will be described next.

To facilitate generalizability, the polygon generation procedure adopted is fundamentally angle based rather than coordinate based. To this end, the radius of the circumcircle and the number of sides are taken as the primary inputs for generating the vertex coordinates. The starting point is a regular reference polygon inscribed in a circle of radius r_c. For regular polygons, the angular positions are regular and defined by the central angle β_{reg} between two consecutive radii connecting adjacent vertices, which is identical for all n angles. In the case of irregular polygons, a smooth perturbation of each vertex angle is introduced to modify their values. This perturbation is controlled through an irregularity index (II), which ranges from 0 to 100 percent. A value of 0 produces a regular polygon, while a value of 100 percent leads to an extremely distorted shape. In the present study, rolling blocks with irregularity indices of up to 50 percent (or 0.50) are studied.

The random number generator function `randn` implemented in Matlab [27] is used to generate n random values, where the randomness is statistical rather than fundamental and is therefore reproducible through control of the initial internal state by specifying a seed. The function `randn` generates values from a normal distribution with zero mean and unit standard deviation and uses deterministic algorithms, such as the Mersenne Twister and Ziggurat methods [50, 51], to emulate randomness. As a result, the generated sequence is pseudo random rather than truly random. This implies that `randn` is deterministic once initialized, statistically reliable, and well tested for scientific applications [52]. The function `rng(seed)` is used to control the state of MATLAB's random number generator by setting the internal state to a reproducible configuration determined by the integer `seed`. This ensures reproducibility, since the same seed produces the same sequence of random numbers. The new angular positions are then obtained as

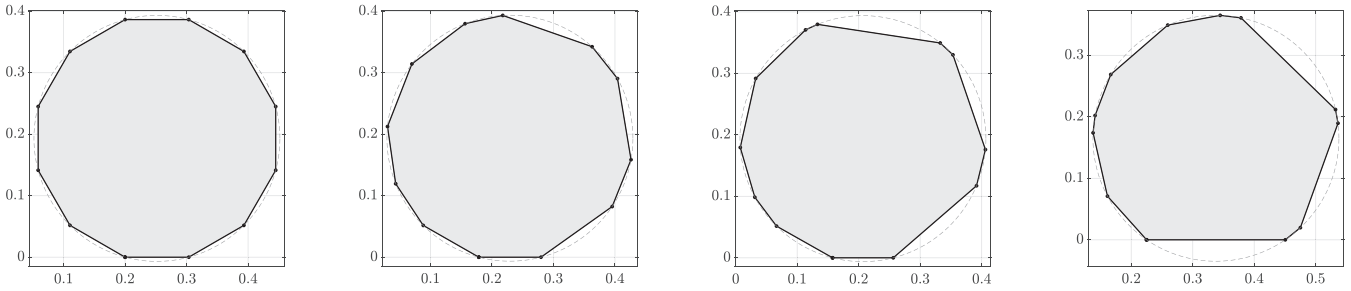
$$\beta = \beta_{reg} + \sigma * \texttt{randn}(1, n), \text{ with } \sigma = II \cdot \frac{2\pi}{n} \tag{37}$$

where β represents the internal angles of an irregular cyclic polygon.

The convexity of the shape is ensured prior to generating the vertex coordinates, which are obtained by converting the polar coordinates to Cartesian coordinates. Before computing the geometrical properties of the convex polygon, it is ensured that the coordinates of all vertices are positive. To determine the centroidal coordinates, area of the polygon, and moment of inertia about any vertex, the vertex coordinates are used in the Shoelace formula, which is a direct consequence of Green's theorem [53, 54].

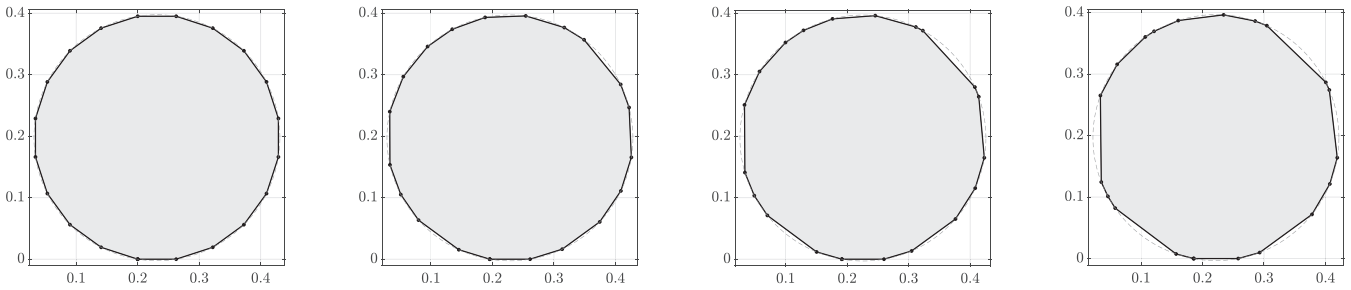
Figures 8 and 9 present representative twelve sided and twenty sided cyclic polygons, respectively, generated with progressively increasing geometric irregularity, II indices of 0 (regular polygon) to 0.50, while preserving the circumradius and number of sides. For both cases, a constant random seed of 5 is used. It should be noted that the choice of seed is arbitrary and has no physical significance. This controlled approach leads to non uniform side lengths and vertex angles, allowing the influence of geometric irregularity on rocking and rolling responses to be examined systematically. The mechanical implication of

10969845, 2026, 12, Downloaded from https://onlinelibrary.wiley.com/doi/10.1002/eqe.70244 by Imperial College London, Wiley Online Library on [12/10/2026]. See the Terms and Conditions (https://onlinelibrary.wiley.com/terms-and-conditions) on Wiley Online Library for rules of use; OA articles are governed by the applicable Creative Commons License



(a) Regular polygon with $n = 12$, $II = 0.0$, seed = 5 (b) Low irregularity with $n = 12$, $II = 0.15$, seed = 5 (c) Medium irregularity $n = 12$, $II = 0.30$, seed = 5 (d) High irregularity with $n = 12$, $II = 0.50$, seed = 5

FIGURE 8 | Examples of 12 sided cyclic polygons with the same circumradius and increasing geometric irregularity. From left to right, the regular case and three levels of irregularity with constant seed are shown.



(a) Regular polygon with $n = 20$, $II = 0.0$, seed = 5 (b) Low irregularity with $n = 20$, $II = 0.15$, seed = 5 (c) Medium irregularity $n = 20$, $II = 0.30$, seed = 5 (d) High irregularity with $n = 20$, $II = 0.50$, seed = 5

FIGURE 9 | Examples of 20 sided cyclic polygons with the same circumradius and increasing geometric irregularity. From left to right, the regular case and three levels of irregularity with constant seed are shown.

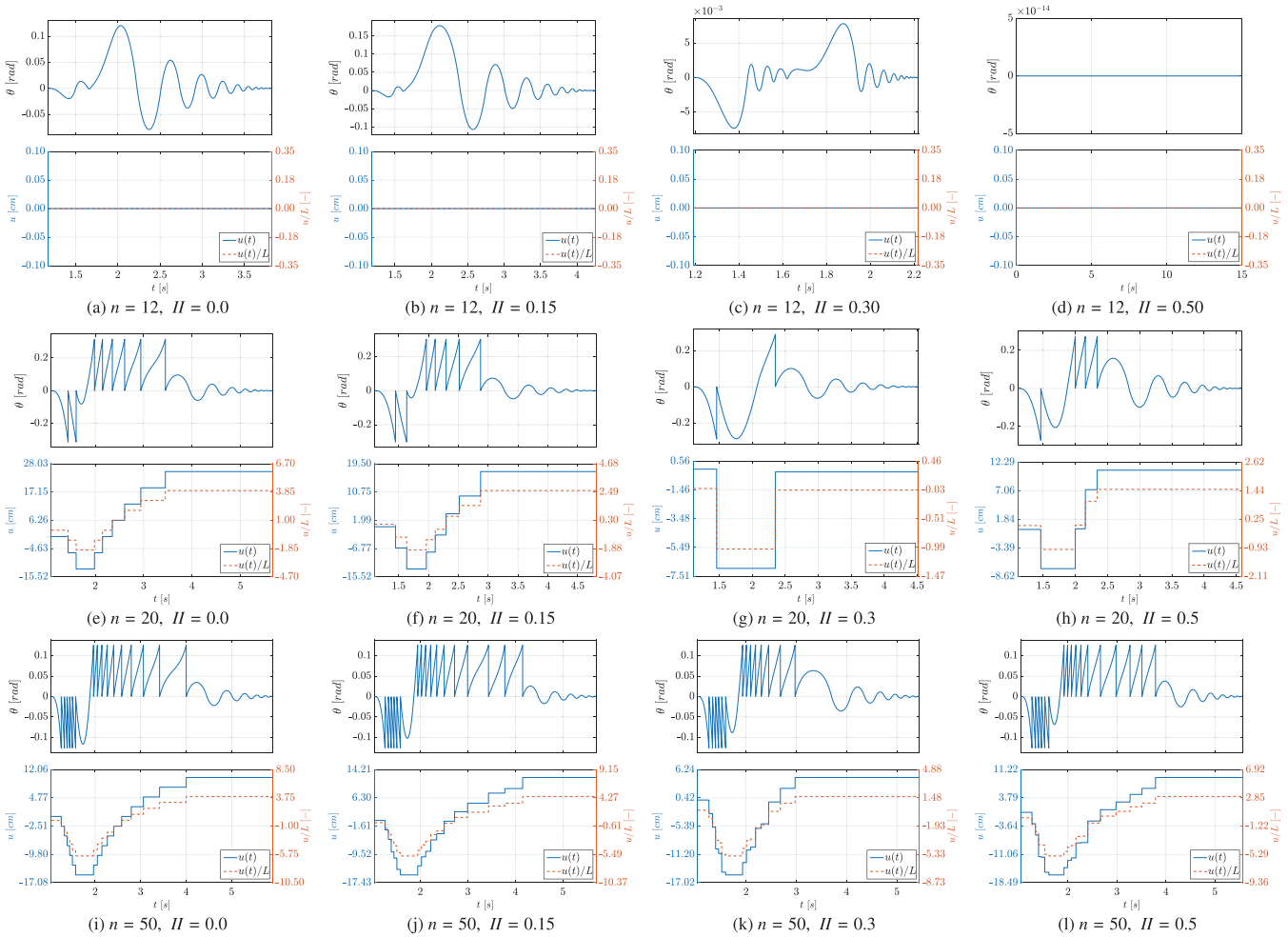
increasing irregularity is the loss of symmetry in pivot geometry. Unlike regular polygons, where successive pivot transitions occur at uniform angular increments, irregular polygons exhibit asymmetric rolling thresholds and pivot dependent frequency parameters. Consequently, impact timing and admissible rolling sequences become irregularity-dependent, even when the global circumradius and number of sides remain fixed. As shown in the response histories presented in Figures 8 and 9, increasing irregularity perturbs the periodicity of rocking cycles, modifies impact sequencing, and alters displacement accumulation. These changes arise purely from geometric asymmetry rather than from any modification of mass or excitation intensity.

To further examine the consequences of geometric asymmetry, Figure 10 presents representative response histories of rotation, cumulative displacement, and normalized cumulative horizontal displacement for $n = 12$, $n = 20$, and $n = 50$ polygons with increasing irregularity index subjected the same base excitation formed by a sine pulse with amplitude $a_p = 0.3$g and frequency $\omega_p = 2\pi$ rad/s. L is used for normalization of displacements in this figure and denotes the side length of the cyclic polygon. In the case of irregular polygons, L is measured between the two successive vertices laying horizontally on the ground at the beginning of the motion. Thus, L is used only as a practical geometric normalization factor. For the regular configuration ($II = 0$) the rocking response exhibits near symmetric excursions about the reference orientation. As the irregularity index increases, this mild response symmetry is progressively lost and the peak rotations in clockwise and counterclockwise directions no longer coincide. Also, uplift initiation and rolling transitions occur at different angular magnitudes depending on direction. In general, the response histories reveal unequal rocking envelopes and visibly non periodic impact sequences

In its present formulation, our model captures the local gravitational restoring action associated with each rocking phase. However, the system does not include an independent global restoring mechanism that would ensure re-centring after cumulative rolling has occurred making it prone to considerable residual displacements at large ground-motion intensities. However, as noted before, when the cyclic polygon approaches the circular shape, other phenomena like friction and deformability, which are not accounted herein, can take precedence.

For moderate irregularity, the system exhibits directional bias. Rolling events accumulate preferentially in one direction due to the unequal geometric thresholds. The magnitude of this drift increases with irregularity and is particularly pronounced for lower sided polygons such as $n = 12$, where each pivot transition represents a larger geometric reconfiguration. For higher sided polygons such as $n = 50$, the influence of irregularity remains but is attenuated. Because the angular increment between adjacent vertices is small, the geometric perturbations introduced by irregularity are distributed over many potential pivots. As a result, the rocking envelopes remain comparatively smooth and the cumulative displacement grows more gradually. Nevertheless, even at large n, asymmetry in pivot dependent parameters produces measurable deviation from the regular case. Figure 10 demonstrates that irregularity does not merely

10969845, 2026, 12, Downloaded from https://onlinelibrary.wiley.com/doi/10.1002/eqe.70244 by Imperial College London, Wiley Online Library on [12/10/2026]. See the Terms and Conditions (https://onlinelibrary.wiley.com/terms-and-conditions) on Wiley Online Library for rules of use; OA articles are governed by the applicable Creative Commons License

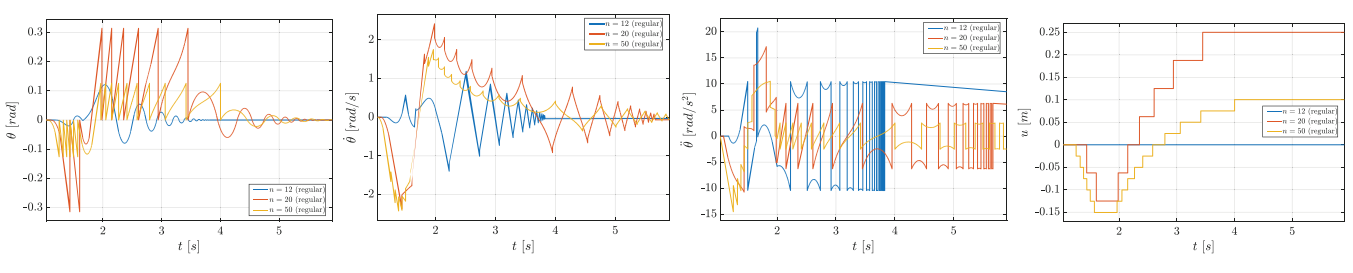


(a) $n = 12,\ II = 0.0$ (b) $n = 12,\ II = 0.15$ (c) $n = 12,\ II = 0.30$ (d) $n = 12,\ II = 0.50$

(e) $n = 20,\ II = 0.0$ (f) $n = 20,\ II = 0.15$ (g) $n = 20,\ II = 0.3$ (h) $n = 20,\ II = 0.5$

(i) $n = 50,\ II = 0.0$ (j) $n = 50,\ II = 0.15$ (k) $n = 50,\ II = 0.3$ (l) $n = 50,\ II = 0.5$

FIGURE 10 | Response histories of rotation, θ, and cumulative horizontal displacement, u, for cyclic polygons with $n = 12, 20$, and 50 and increasing irregularity index $II = 0.00, 0.15, 0.30$, and 0.50; subjected to a sine pulse with $a_p = 0.3g$ and $\omega_p = 2\pi$ rad/s. In each panel, the bottom subplot shows the dimensional cumulative horizontal displacement, $u(t)$, in cm on the left vertical axis and the normalized cumulative horizontal displacement, $u(t)/L$, on the independently scaled right vertical axis. Here, L denotes the side length of the cyclic polygon and is used for displacement normalization (shown in red). Each row corresponds to a fixed n, while each column corresponds to increasing irregularity.



(a) (b) (c) (d)

FIGURE 11 | Regular cyclic polygons with $n = 12, 20, 50$ subjected to a sine pulse excitation with $a_p = 0.3g$ and $\omega_p = 2\pi$ rad/s: (a) rotation response, $\theta(t)$, (b) angular velocity response, $\dot{\theta}(t)$, (c) angular acceleration response, $\ddot{\theta}(t)$, and (d) horizontal displacement, $u(t)$.

perturb but modifies the sequence and magnitude of rocking and rolling events. The dynamic response therefore becomes history dependent and direction sensitive, even under symmetric excitation. This confirms that geometric irregularity introduces an intrinsic bias in energy dissipation and rolling accumulation through asymmetric pivot activation.

Figures 11, 12, and 13 introduce the response histories of rigid polygones subjected to uniform pulse excitations in order to examine the effect of the number of sides, geometric irregularity, and vertex distribution on the dynamic behaviour of the system. These figures demonstrate that the contact kinematics are the main governing factor of the transition from rocking to rolling.

10969845, 2026, 12, Downloaded from https://onlinelibrary.wiley.com/doi/10.1002/eqe.70244 by Imperial College London, Wiley Online Library on [12/10/2026]. See the Terms and Conditions (https://onlinelibrary.wiley.com/terms-and-conditions) on Wiley Online Library for rules of use; OA articles are governed by the applicable Creative Commons License

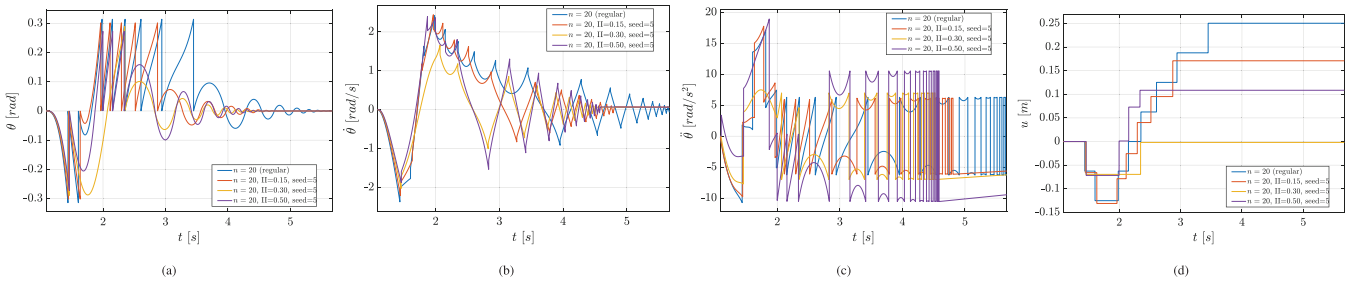


FIGURE 12 | Irregular cyclic polygons of fixed $n = 20$ and seed = 5, and varying the irregularity index (II), subjected to a sine pulse excitation with $a_p = 0.3g$ and $\omega_p = 2\pi$ rad/s: (a) rotation response, $\theta(t)$, (b) angular velocity response, $\dot{\theta}(t)$, (c) angular acceleration response, $\ddot{\theta}(t)$, and (d) horizontal displacement, $u(t)$.

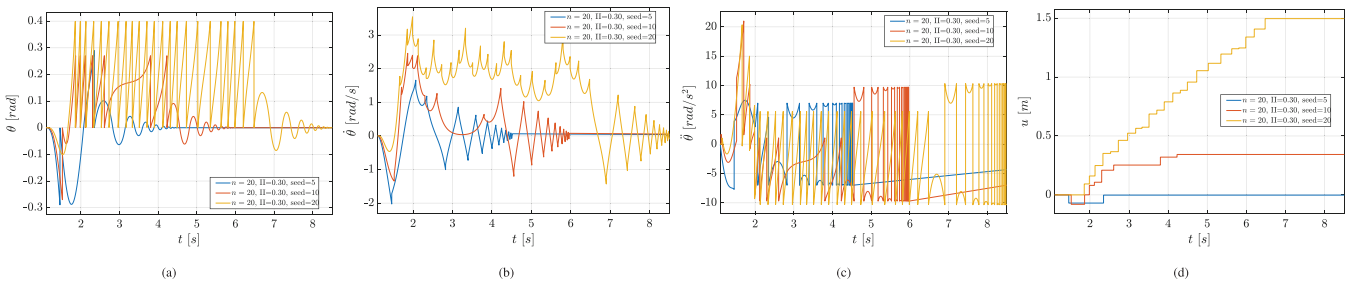


FIGURE 13 | Irregular cyclic polygons of fixed $n = 20$ and $\Pi = 0.30$, and varying the random seed, subjected to a sine pulse excitation with $a_p = 0.3g$ and $\omega_p = 2\pi$ rad/s: (a) rotation response, $\theta(t)$, (b) angular velocity response, $\dot{\theta}(t)$, (c) angular acceleration response, $\ddot{\theta}(t)$, and (d) horizontal displacement, $u(t)$.

As noted above, as the number of sides n increases, the peak rotational excursions reduce because pivot-switching and rolling events increase, which leads to smoother rotational histories. There are more acceleration spikes, but they are evenly spaced, and thus the cumulative horizontal displacement is greater due to continuous pivot migration. The rotation histories differ between seeds and the timing of impacts also changes. The angular velocity and acceleration show similar variations whilst the horizontal displacement accumulates at different rates. These results highlight the sensitivity of the rocking and rolling response to local geometric variations, even within similar irregularity levels.

4 | Response Measures and Non-Dimensional Parameters

In this section a dimensional analysis of the governing equation for the rocking and rolling response of a single rigid regular polygon supporting a rigid superstructure of mass m_{sup} is presented. The objective is to identify the fundamental non-dimensional groups that control the dynamics of the system and to reduce the dependence of the response to a minimal set of governing parameters. This approach follows the classical methodology of Vaschy [55] and Buckingham [56] as discussed in Barenblatt [57], in which the physical problem is recast in terms of dimensionless quantities whose behaviour is invariant under a change of fundamental measurement units.

The peak rotational response, $\max|\theta(t)|$, or the total permanent net cumulative rotational response (residual) at the end of the motion, $|\theta_{\text{net}}(t_f)|$, of the system under study when subjected to a base motion of acceleration amplitude, a_p, and characteristic frequency, ω_p, is a function of the following parameters (see Figure 3b):

$$\max|\theta(t)| = f\left(\gamma, r_c, \phi, g, a_p, \omega_p, \nu\right) \tag{38}$$

or, in its more compact form described by Equation (24), in terms of the frequency parameter p defined in Equation (25):

$$\max|\theta(t)| = f\left(p, \phi, g, a_p, \omega_p, \nu\right) \tag{39}$$

Applying Vaschy-Buckingham's Π-theorem [56] the number of independent parameters required to define a unique response can be reduced to four:

$$\frac{\max|\theta(t)|}{\phi} = f\left(\frac{\omega_p}{p}, \frac{a_p}{g}, \phi, \nu\right) \tag{40}$$

It can be appreciated from Equation (40) that the inclusion of multiple sides and pivoting points only modifies the frequency parameter, p. However, in the case of rigid cyclic polygons of multiple sides, the inclusion of alternative pivoting paths adds an additional source of nonlinearity to the equation of motion. This can be considered by adding the number of sides, n, which is a dimensionless-orientationless quantity and can be treated as an independent parameter such that:

$$\frac{\max|\theta(t)|}{\phi} = f\left(\frac{\omega_p}{p}, \frac{a_p}{g}, \phi, \nu, n\right) \tag{41}$$

The central implication is that the response of rolling polygons does not depend on the absolute values of r_c, M_{polygon}, or m_{sup}

10969845, 2026, 12, Downloaded from https://onlinelibrary.wiley.com/doi/10.1002/eqe.70244 by Imperial College London, Wiley Online Library on [12/10/2026]. See the Terms and Conditions (https://onlinelibrary.wiley.com/terms-and-conditions) on Wiley Online Library for rules of use; OA articles are governed by the applicable Creative Commons License

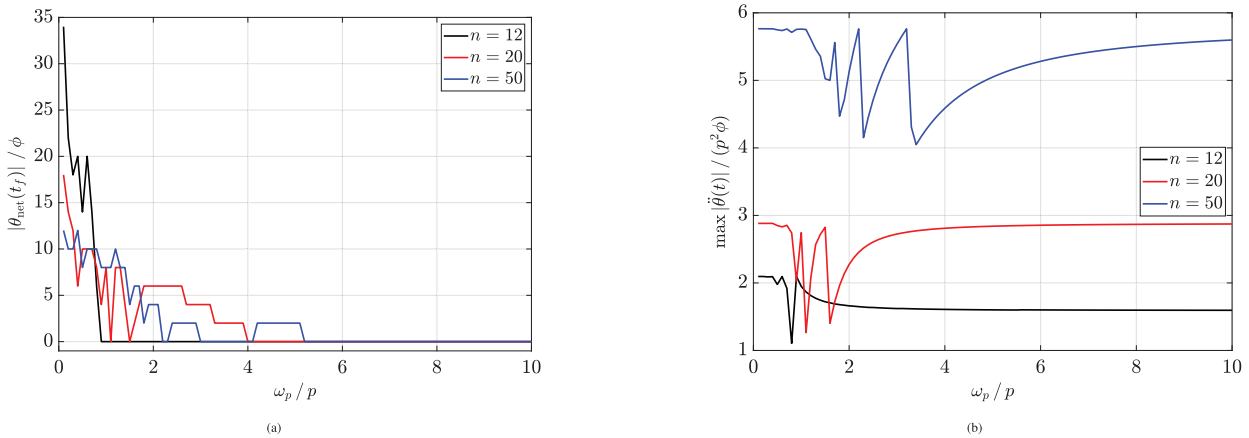


FIGURE 14 | Dimensionless response of regular cyclic polygons subjected to a sine pulse with $a_p = 0.3g$: (a) final normalized cumulative rotation $|\theta_{\text{net}}(t_f)|/\phi$, and (b) normalized peak angular acceleration $\max|\ddot{\theta}(t)|/(p^2\phi)$, plotted against the frequency ratio ω_p/p. The low frequency response is characterized by rolling with discrete plateau like changes in the final cumulative rotation, whereas the high frequency response tends towards re-centring with negligible residual rotation. The angular acceleration demand remains finite across the frequency range considered.

directly, but only through their appearance in the dimensionless groups ω_p/p and n. This drastically simplifies the parametric exploration of the system, reducing a high dimensional physical problem to a few parameter family of curves per given family of n-sided polygons with the same irregularity, II, that has throughout been assumed as a constant independent variable.

Figure 14a reveals how the relative maximum rotation depends on the frequency content of the pulse, while the Figure 14b portrays how the magnitude of the excitation influences the normalized rotation. These plots fully characterize the behaviour of the system and provide a rigorous, dimensionally consistent framework for comparing different geometries, masses, and excitation characteristics within a single unified representation. Furthermore, in Figure 14, two distinct response regimes can be identified. At low values of ω_p/p, the excitation timescale is long compared to the intrinsic timescale of the rolling system. In this regime, the cyclic polygon has sufficient time within a single pulse to uplift, undergo multiple impacts, and transition between successive pivot points. As a result, the system accumulates finite net reorientation. The quantity $|\theta_{\text{net}}(t_f)|/\phi$, therefore, reaches large values. The response varies in a non-smooth manner, consisting of plateaus separated by discrete jumps. This step-like structure reflects the non-smooth kinematics of the system. Since the net rotation is governed by the cumulative geometric reorientation associated with pivot switching, the response is inherently quantized rather than continuous.

With increasing ω_p/p, a transition is observed beyond which $|\theta_{\text{net}}(t_f)|/\phi$ reduces to zero. In this high-frequency regime, the excitation reverses direction before the body can complete sustained rolling or migrate to a new pivot. Rocking and impact events may still occur, but they are followed by re-centring within the same pulse, resulting in negligible net reorientation. The critical transition frequency ratio is polygon dependent. Polygons with larger n maintain non-zero net rotation over a wider frequency range indicating that a higher number of sides facilitate pivot migration when excited by faster pulses. In contrast, the dimensionless peak angular acceleration remains finite over the entire frequency range. Even in the regime where no rolling events occurring, significant angular accelerations are observed due to uplift and impact events. This demonstrates that the absence of residual rotation does not imply the absence of dynamic amplification. The acceleration demand is sensitive to the intensity and timing of impacts. Interestingly, higher n polygons exhibit larger normalized acceleration levels, which may be attributed to more frequent pivot switching intervals of shorter duration.

5 | Response of Cyclic Polygons to Real Pulse-Like Ground Motions

Previous sections have focused on the response of cyclic polygonal bodies subjected to idealised pulses. This allowed the fundamental mechanisms governing uplift, rocking, impact, and rolling to be examined in a controlled and physically transparent manner. While such fully coherent excitations are valuable for isolating key parameters and response regimes, recorded near-field earthquake motions are characterised by a more complex temporal structure. In addition to coherent long-period velocity pulses, real ground motions often contain high-frequency fluctuations and acceleration spikes that may significantly influence the initiation of uplift, the sequence of pivot switching events, and the cumulative rolling response of rigid body isolation systems. In this section, the proposed framework is extended to the analysis of real pulse-like ground motions. A set of 201 recorded near-field ground motion records is employed, selected from the Pacific Earthquake Engineering Research Center [58]database. The records correspond to 26 earthquakes with moment magnitudes M_w ranging from 5.4 to 7.9, thereby covering a broad spectrum of pulse-dominated seismic events. The catalogue of selected earthquake records and their key characteristics are summarised in Table 1.

5.1 | Non-Dimensional Intensity Measures

A key challenge in assessing the rocking and rolling response of cyclic polygons under real earthquake ground motions is

10969845, 2026, 12, Downloaded from https://onlinelibrary.wiley.com/doi/10.1002/eqe.70244 by Imperial College London, Wiley Online Library on [12/10/2026]. See the Terms and Conditions (https://onlinelibrary.wiley.com/terms-and-conditions) on Wiley Online Library for rules of use; OA articles are governed by the applicable Creative Commons License

TABLE 1 | Earthquake records used in this study.

Earthquake	Magnitude M_w	Fault mechanism	Year	No. of records
Cape Mendocino	7.01	Reverse	1992	4
Chi Chi Taiwan	7.62	Reverse Oblique	1999	56
Chi Chi Taiwan 04	6.2	Strike slip	1999	2
Chi Chi Taiwan 06	6.3	Reverse	1999	2
Chuetsu oki	6.8	Reverse	2007	2
Coyote Lake	5.74	Strike slip	1979	8
Darfield New Zealand	7.0	Strike slip	2010	20
Denali Alaska	7.9	Strike slip	2002	2
Duzce Turkey	7.14	Strike slip	1999	2
Imperial Valley 06	6.53	Strike slip	1979	18
Irpinia Italy 01	6.9	Normal	1980	4
Kalamata Greece 02	5.4	Normal	1986	2
Kobe Japan	6.9	Strike slip	1995	6
Kocaeli Turkey	7.51	Strike slip	1999	8
Landers	7.28	Strike slip	1992	2
Loma Prieta	6.93	Reverse Oblique	1989	10
Montenegro Yugo.	7.1	Reverse	1979	2
Morgan Hill	6.19	Strike slip	1984	4
Niigata Japan	6.63	Reverse	2004	4
Northridge 01	6.69	Reverse	1994	10
Parkfield 02 CA	6.0	Strike slip	2004	20
San Salvador	5.8	Strike slip	1986	4
Superstition Hills 02	6.54	Strike slip	1987	4
Tabas Iran	7.35	Reverse	1978	2
Tottori Japan	6.61	Strike slip	2000	2
Westmorland	5.9	Strike slip	1981	2

the selection of intensity measures that correlate reliably with structural demand. This task is particularly challenging due to the strongly nonlinear and non-smooth responses of these systems. Uplift initiation, impacts, and pivot switching are all sensitive to both acceleration and velocity characteristics of the excitation [59]. Previous studies have shown that rocking response is strongly influenced by peak ground velocity and peak ground acceleration. This has led to the use of several dimensionless intensity measures normalised by the uplift threshold, such as $p\mathrm{PGV}/(g\tan\alpha)$ and $\mathrm{PGA}/(g\tan\alpha)$ [60, 61]. Petrone et al. [62] demonstrated that velocity based intensity measures correlate more effectively with rocking demands for large scale structures. In contrast, acceleration based measures tend to perform better for smaller and more compact bodies. Beyond amplitude related measures, several researchers have highlighted the importance of ground motion duration and temporal characteristics in governing rocking response and overturning potential [3, 63, 64]. Motivated by these findings, and consistent with the analytical formulation adopted in this study, the dimensionless intensity measure pt_{uni} is employed to characterise seismic demand, where t_{uni} is the uniform duration of the record as shown in Figure 15. This intensity measure captures the interaction between the characteristic time scale of the excitation [65] and the frequency parameter of the rocking polygon. It is therefore well suited for assessing maximum rotation and angular acceleration in stable rocking and rolling regimes.

5.2 | Seismic Demand Analysis

A cloud based seismic demand analysis is performed using the set of earthquake ground motions listed in Table 1. The objective of this analysis is to quantify the seismic demand imposed on cyclic polygonal systems when subjected to real pulse-like ground motions. Three regular cyclic polygons with $n = 12, 20$ and 50 are selected as representative case studies for the examination of the influence of polygon resolution on peak rotational response and angular acceleration demand.

Consistent with the response measures introduced in Section 4, structural demand is characterised using the normalised peak rotation, $|\theta_{\mathrm{net}}(t_f)|/\phi$, and the normalised peak angular acceleration, $\max|\ddot{\theta}(t)|/p^2\phi$. These dimensionless quantities allow a

10969845, 2026, 12, Downloaded from https://onlinelibrary.wiley.com/doi/10.1002/eqe.70244 by Imperial College London, Wiley Online Library on [12/10/2026]. See the Terms and Conditions (https://onlinelibrary.wiley.com/terms-and-conditions) on Wiley Online Library for rules of use; OA articles are governed by the applicable Creative Commons License

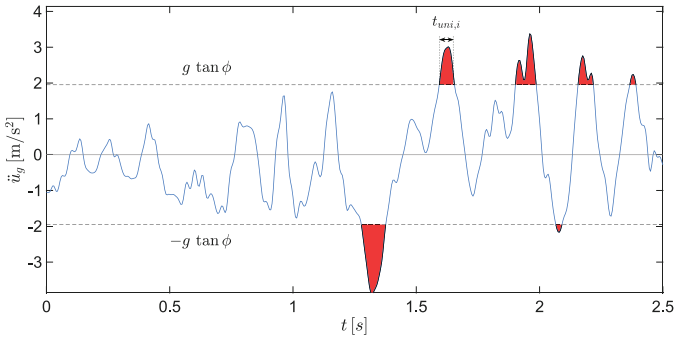


FIGURE 15 | Definition and illustration of the uplift exceedance periods, $t_{uni,i}$, whose summation determines the ground motion time scale, $t_{uni} = \sum_{i=1}^{j} t_{uni,i}$ used in this study for the formulation of the compounded intensity measure, pt_{uni}.

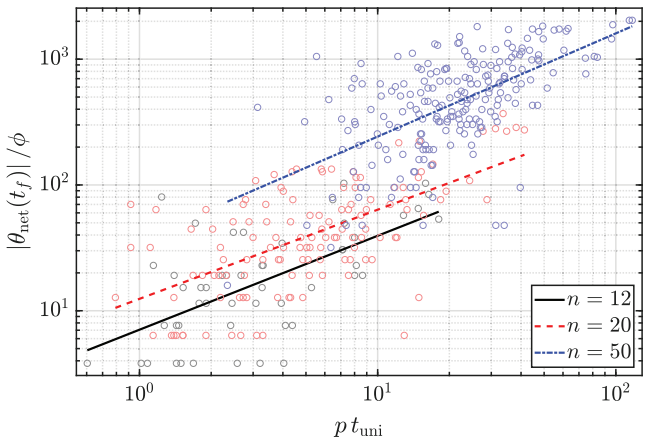


FIGURE 16 | Cloud analysis and fitted power law model for final normalized cumulative rotation versus the dimensionless intensity measure pt_{uni} for regular cyclic polygons with varying number of sides n and constant circumradius r_c.

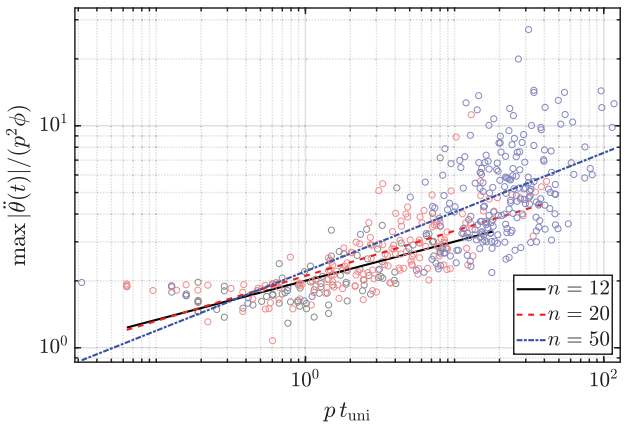


FIGURE 17 | Cloud analysis and fitted power law model for normalized peak acceleration versus the dimensionless intensity measure pt_{uni} for regular cyclic polygons with varying number of sides n and constant circumradius r_c.

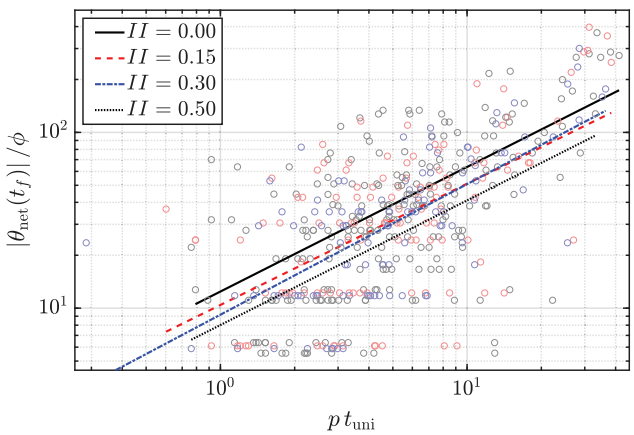


FIGURE 18 | Cloud analysis and fitted power law model for final normalized cumulative rotation versus the dimensionless intensity measure pt_{uni} for irregular cyclic polygons with fixed $n = 20$ and increasing irregularity index.

direct comparison of demand across different excitation intensities and geometric configurations.

In probabilistic seismic demand modelling, it is commonly assumed that the median structural demand, $(\bar{D}_m)$, follows a power law relationship with the selected intensity measure, IM [66, 67]. This relationship can be expressed as

$$\bar{D}_m = a\mathrm{IM}^b \tag{42}$$

where a is the intercept or demand level at unit intensity and b is the scaling exponent. Both of these parameters are obtained through regression analysis. Taking the natural logarithm of both sides yields a linear relationship in logarithmic space, given by

$$\ln(\bar{D}_m) = \ln(a) + b\ln(\mathrm{IM}) \tag{43}$$

which enables straightforward estimation of the model coefficients using linear regression.

The results of the cloud analysis for the regular and irregular polygonal configurations are depicted in Figures 16–19 together with the fitted seismic demand models for normalised cumulative permanent rotation and peak angular acceleration. For regular polygons, the coefficient b of the linear trends for cumulative permanent rotation exponents vary from approximately 0.70 to 0.83 depending on the number of sides, n (Figure 16). In the case of irregular polygons, b is around 0.70 (Figure 18). This suggests that duration governs the growth mechanism of residual cumulative rotation. On the other hand, the coefficient a increases strongly with the number of sides, n, in regular polygons (from 7.05 for $n =$ 12 to 35.61 for $n = 50$ in Figure 16). This indicates that the polygon

10969845, 2026, 12, Downloaded from https://onlinelibrary.wiley.com/doi/10.1002/eqe.70244 by Imperial College London, Wiley Online Library on [12/10/2026]. See the Terms and Conditions (https://onlinelibrary.wiley.com/terms-and-conditions) on Wiley Online Library for rules of use; OA articles are governed by the applicable Creative Commons License

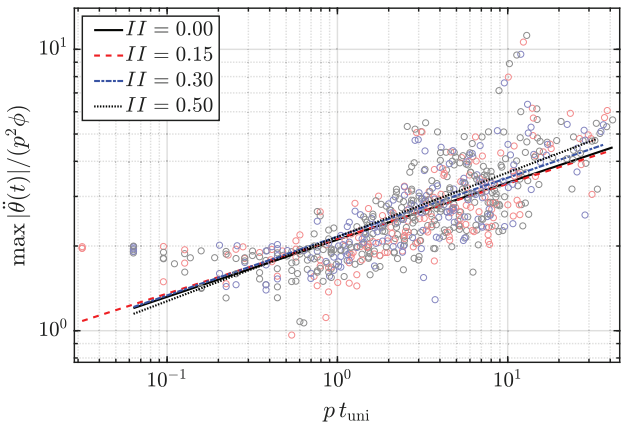


FIGURE 19 | Cloud analysis and fitted power law model for normalized peak acceleration versus the dimensionless intensity measure pt_{uni} for irregular cyclic polygons with fixed $n = 20$ and increasing irregularity index.

resolution can shift the total residual translation of the isolation system, even if the overall scaling behaviour remains similar, while a tendency for more irregular polygons to accumulate lower residual deformations is observed in Figure 18.

In terms of normalized peak accelerations, shown in Figures 17 and 19, the regression analyses depict smaller exponents, with b values ranging from $0.18 - 0.27$ in case of regular polygons and from $0.20 - 0.22$ for irregular ones. Larger IMs are also associated with greater scatter. The trends across different resolution and irregularity levels are almost overlapping which suggests that peak acceleration is comparatively insensitive to geometric irregularity. It is instead governed primarily by impact mechanics and restitution controlled velocity changes, as elaborated in the previous sections of this paper. These results collectively show that pt_{uni} is an effective organiser of peak rotation demand across cyclic polygon families, while peak acceleration remains more strongly influenced by discrete impact events than by smooth duration scaling.

Given the fundamental nature of our formulation, the following limitations can be mentioned. First, the current rigid-body idealization does not account for local contact compliance, surface damage, or degradation effects associated with repeated high-speed rolling impacts, phenomena that are known to reduce the reliability of analytical predictions [68]. In addition, the influence of bidirectional loading should be investigated in future studies. These limitations do not diminish the analytical value of the present work; but they clearly define its scope as a first analytical baseline study linking geometry and irregularity to rocking and rolling kinematics upon which further investigations can be made.

6 | Conclusion

This study has examined the rocking and rolling response of regular and irregular rigid polygons subjected to base excitation. Such systems can be interpreted as first-order approximations to the fundamental dynamics governing ideal kinematic isolation layers. We present an event-driven analytical framework that describes the uplift, impact, and successive pivot switching transitions as mechanically consistent events within a single formulation.

The governing equation of motion together with the associated uplift initiation criterion for the rigid polygon layer holding a rigid superstructure is obtained from variational principles. We show that the motion of cyclic polygons is a generalization of the rocking body response that formalizes the transitions to neighbouring pivot vertices as admissible kinematic events with a modified frequency parameter p. The central implication is that the response of rolling polygons does depend on the absolute values of their circumradius, r_c, their mass, M_{polygon}, the mass of the superstructure, m_{sup}, or the number of polygons in the isolation layer, but only through their appearance within the de p parameter. Hence stressing the central roles of geometry and inertia as mechanisms for designing the dynamic response of rolling isolation systems. The mass-independence of the uplift acceleration threshold is also confirmed, establishing polygon geometry, through ϕ, as the primary design variable for tuning isolation activation.

We also demonstrate that polygon resolution strongly shapes the response regime. As the number of sides increases, the uplift threshold decreases (i.e., ϕ reduces), and the system becomes more readily activated. At the same time, the peak rotation tends to decrease with increasing resolution for a given pulse intensity, while horizontal displacement can accumulate through repeated pivot switching. This supports the central interpretation of the study. Similarly, irregularity alters the timing of impacts and the progression of pivot switching. This leads to measurable changes in rotation peaks, acceleration spikes, and cumulative displacement, even when the circumradius and the number of sides are held constant. A tendency of irregular polygons to accumulate lower residual translations has also been documented. These observations explain how local geometric variations, not only global resolution, influence whether the response is dominated by bounded rocking or by progressive rolling. Peak normalized acceleration increases as the number of sides, n, increases which may be attributed to more frequent pivot switching of shorter duration which also leads to larger cumulative horizontal displacement.

Our analyses were extended to real recorded pulse-like ground motions. A cloud based demand analysis reinforced our initial findings on how polygon resolution and irregularity influence seismic demands under a diverse record set. The cumulative rotational demand increased strongly with the number of sides, n, indicating that the polygon resolution can shift the demand level, even if the overall scaling behaviour remains similar. The relationships between cyclic polygon resolution and kinematics with the overall response identified in this study provide a preliminary rational basis for designing rigid body rocking-rolling isolation systems and has implications for architected geometry-driven protective systems.

Conflicts of Interest

The authors declare no conflicts of interest.

10969845, 2026, 12, Downloaded from https://onlinelibrary.wiley.com/doi/10.1002/eqe.70244 by Imperial College London, Wiley Online Library on [12/10/2026]. See the Terms and Conditions (https://onlinelibrary.wiley.com/terms-and-conditions) on Wiley Online Library for rules of use; OA articles are governed by the applicable Creative Commons License

Data Availability Statement

Data supporting this study are archived at Zenodo DOI: 10.5281/zenodo.21308482 and are maintained in the GitHub repository: https://github.com/CMalagaC/RigidPolygonDynamics.

References

1. N. Makris and M. F. Vassiliou, "Planar Rocking Response and Stability Analysis of an Array of Free-Standing Columns Capped With a Freely Supported Rigid Beam," *Earthquake Engineering & Structural Dynamics* 42, no. 3 (2013): 431–449, https://onlinelibrary.wiley.com/doi/abs/10.1002/eqe.2222.

2. N. Makris and Y. S. Roussos, "Rocking Response of Rigid Blocks Under Near-Source Ground Motions," *Géotechnique* 50, no. 3 (2000): 243–262, https://doi.org/10.1680/geot.2000.50.3.243.

3. G. W. Housner, "The Behavior of Inverted Pendulum Structures During Earthquakes," *Bulletin of the Seismological Society of America* 53, no. 2 (1963): 403–417.

4. K. E. Bantilas, I. E. Kavvadias, and L. K. Vasiliadis, "Analytical Investigation of the Seismic Response of Elastic Oscillators Placed on the Top of Rocking Storey," *Bulletin of Earthquake Engineering* 19, no. 2 (2021): 1249–1270, https://doi.org/10.1007/s10518-020-01019-3.

5. Z.-Y. Zhang, M. N. Chatzis, and S. Acikgoz, "The Dynamic Behaviour of Flexible Oscillators Rocking and Sliding on Concentrated Springs," *Earthquake Engineering & Structural Dynamics* 53, no. 11 (2024): 3405–3426.

6. A. M. D'Altri, G. Vlachakis, S. de Miranda, and P. B. Lourenço, "Rocking Block Simulation Based on Numerical Dissipation," *Nonlinear Dynamics* 112, no. 20 (2024): 17843–17862, https://doi.org/10.1007/s11071-024-09974-1.

7. S. Belliazzi, G. P. Lignola, and E. Cosenza, "Numerical Analysis for the Response to Rocking of Asymmetric Bodies," in *3rd International Conference on International Conference on Recent Advances in Nonlinear Design, Resilience and Rehabilitation of Structures, CoRASS*, CoRASS. (Coimbra, Portugal: 3rd International Conference on Recent Advances in Nonlinear Design, Resilience and Rehabilitation of Structures, CoRASS, 2019), https://www.researchgate.net/publication/339617977_Numerical_analysis_for_the_response_to_rocking_of_asymmetric_bodies.

8. B. Huang, S. Günay, and W. Lu, "Seismic Assessment of Freestanding Ceramic Vase With Shaking Table Testing and Performance-Based Earthquake Engineering," *Journal of Earthquake Engineering* 26, no. 15 (2022): 7956–7978, https://doi.org/10.1080/13632469.2021.1979132.

9. L. Berto, L. Di Sarno, M. Fragiadakis, I. Rocca, and A. Saetta, "Seismic Assessment of Free-Standing Artifacts: Full-Scale Tests on Large Shake Table," *Earthquake Engineering & Structural Dynamics* 52, no. 9 (2023): 2708–2730, https://onlinelibrary.wiley.com/doi/abs/10.1002/eqe.3890.

10. C.-S. Yim, A. K. Chopra, and J. Penzien, "Rocking Response of Rigid Blocks to Earthquakes," *Earthquake Engineering & Structural Dynamics* 8, no. 6 (1980): 565–587, https://onlinelibrary.wiley.com/doi/abs/10.1002/eqe.4290080606.

11. H. Liu, Y. Huang, and X. Liu, "Seismic Overturning Fragility Analysis for Rigid Blocks Subjected to Floor Motions," *Sustainability* 15, no. 6 (2023): 4945, https://www.mdpi.com/2071-1050/15/6/4945.

12. J. M. Kelly and D. F. Tsztoo, "Earthquake Simulation Testing of a Stepping Frame With Energy-Absorbing Devices," *New Zealand Society for Earthquake Engineering* 10 (1977): 196–207, https://bulletin.nzsee.org.nz/index.php/bnzsee/article/view/1132.

13. A. Palmeri and N. Makris, "Linearization and First-Order Expansion of the Rocking Motion of Rigid Blocks Stepping on Viscoelastic Foundation," *Earthquake Engineering & Structural Dynamics* 37, no. 7 (2008): 1065–1080, https://onlinelibrary.wiley.com/doi/abs/10.1002/eqe.799.

14. G. C. Tsiatas, A. E. Charalampakis, and P. Tsopelas, "A Subbuteo-Inspired Rolling Isolation System for Protecting Rigid Blocks," *Earthquake Engineering & Structural Dynamics* 54, no. 7 (2025): 1918–1933, https://onlinelibrary.wiley.com/doi/abs/10.1002/eqe.4343.

15. D. Foti, "Rolling Devices for Seismic Isolation of Lightweight Structures and Equipment. Design and Realization of a Prototype," *Structural Control and Health Monitoring* 26, no. 3 (2019): e2311, https://onlinelibrary.wiley.com/doi/abs/10.1002/stc.2311.

16. N. Maureira-Carsalade, E. Pardo, C. Oyarzo-Vera, and A. Roco, "A Roller Type Base Isolation Device With Tensile Strength," *Engineering Structures* 221 (2020): 111003, https://www.sciencedirect.com/science/article/pii/S0141029619334807.

17. A. Rasheed and C. Málaga-Chuquitaype, *Assessment of the Ancient Technology of Wrapped Stones as Low-Cost Seismic Isolation Alternative* (2024).

18. F. Naeim and J. M. Kellu, *Design of Seismic Isolated Structures: From Theory to Practice* (John Wiley & Sons, 1999).

19. I. G. Buckle and R. L. Mayes, "Seismic Isolation: History, Application, and Performance–A World View," *Earthquake Spectra* 6 (1990): 161–201, https://ui.adsabs.harvard.edu/abs/1990EarSp.6.161B.

20. R. I. Skinner, W. H. Robinson, and G. H. McVerry, *An Introduction to Seismic Isolation* (Wiley, 1993).

21. P. S. Harvey and K. C. Kelly, "A Review of Rolling-Type Seismic Isolation: Historical Development and Future Directions," *Engineering Structures* 125 (2016): 521–531, https://www.sciencedirect.com/science/article/pii/S0141029616303595.

22. N. Makris and D. Konstantinidis, "The Rocking Spectrum and the Limitations of Practical Design Methodologies," *Earthquake Engineering & Structural Dynamics* 32, no. 2 (2003): 265–289, https://onlinelibrary.wiley.com/doi/abs/10.1002/eqe.223.

23. B. Brogliato, *Nonsmooth Mechanics: Models, Dynamics and Control*, ser. Communications and Control Engineering (Springer International Publishing, 2016), http://link.springer.com/10.1007/978-3-319-28664-8.

24. J. J. Moreau, "Unilateral Contact and Dry Friction in Finite Freedom Dynamics," in *Nonsmooth Mechanics and Applications*, edited by J. J. Moreau and P. D. Panagiotopoulos, 1–82 (Springer, 1988), https://doi.org/10.1007/978-3-7091-2624-0_1.

25. M. Jean, "The Non-Smooth Contact Dynamics Method," *Computer Methods in Applied Mechanics and Engineering* 177, no. 3 (1999): 235–257, https://www.sciencedirect.com/science/article/pii/S0045782598003831.

26. S. J. Hogan, "On the Dynamics of Rigid-Block Motion Under Harmonic Forcing," *Proceedings of the Royal Society of London, A Mathematical and Physical Sciences* 425, no. 1869 (1989): 441–476, https://doi.org/10.1098/rspa.1989.0114.

27. The MathWorks Inc., "MATLAB Version 25.2 (R2025b)," Computer Software (2025), https://www.mathworks.com.

28. M. Constantinou, A. Mokha, and A. Reinhorn, "Teflon Bearings in Base Isolation II: Modeling," *Journal of Structural Engineering* 116, no. 2 (1990): 455–474, https://doi.org/10.1061/(ASCE)0733-9445(1990)116:2(455).

29. A. Mokha, M. Constantinou, and A. Reinhorn, "Teflon Bearings in Base Isolation I: Testing," *Journal of Structural Engineering* 116, no. 2 (1990): 438–454, https://doi.org/10.1061/(ASCE)0733-9445(1990)116:2(438).

30. H. Cilsalar and M. C. Constantinou, "Behavior of a Spherical Deformable Rolling Seismic Isolator for Lightweight Residential Construction," *Bulletin of Earthquake Engineering* 17, no. 7 (2019): 4321–4345, https://doi.org/10.1007/s10518-019-00626-z.

31. H. Cilsalar and M. C. Constantinou, *Development and Validation of a Seismic Isolation System for Lightweight Residential Construction*, Technical Report MCEER-19-0001 (University at Buffalo, The State University of New York, 2019), https://www.eng.buffalo.edu/mceer-reports/19/19-0001.pdf.

10969845, 2026, 12, Downloaded from https://onlinelibrary.wiley.com/doi/10.1002/eqe.70244 by Imperial College London, Wiley Online Library on [12/10/2026]. See the Terms and Conditions (https://onlinelibrary.wiley.com/terms-and-conditions) on Wiley Online Library for rules of use; OA articles are governed by the applicable Creative Commons License

32. H. Cilsalar and M. C. Constantinou, "Parametric Study of Seismic Collapse Performance of Lightweight Buildings With Spherical Deformable Rolling Isolation System," *Bulletin of Earthquake Engineering* 18, no. 4 (2020): 1475–1498, https://doi.org/10.1007/s10518-019-00753-7.

33. A. A. Katsamakas, L. Del Giudice, S. I. Reyes, D. Candebat-Sanchez, and M. F. Vassiliou, "Experimental and Numerical Assessment of Grout-Filled Tennis Balls as Seismic Isolation Bearings," *Engineering Structures* 294 (2023): 116716.

34. A. A. Katsamakas, G. Belser, M. F. Vassiliou, and M. Blondet, "Experimental Investigation of a Spherical Rubber Isolator for Use in Low Income Countries," *Engineering Structures* 250 (2022): 113522.

35. M. F. Vassiliou and N. Makris, "Estimating Time Scales and Length Scales in Pulselike Earthquake Acceleration Records With Wavelet Analysis," *Bulletin of the Seismological Society of America* 101, no. 2 (2011): 596–618.

36. C. Málaga-Chuquitaype, "Estimation of Peak Displacements in Steel Structures Through Dimensional Analysis and the Efficiency of Alternative Ground-Motion Time and Length Scales," *Engineering Structures* 101 (2015): 264–278.

37. G. Augusti and A. Sinopoli, "Modelling the Dynamics of Large Block Structures," *Meccanica* 27, no. 3 (1992): 195–211, https://doi.org/10.1007/BF00430045.

38. F. Prieto, P. B. Lourenço, and C. S. Oliveira, "Impulsive Dirac-Delta Forces in the Rocking Motion," *Earthquake Engineering & Structural Dynamics* 33, no. 7 (2004): 839–857, https://onlinelibrary.wiley.com/doi/abs/10.1002/eqe.381.

39. C. Yilmaz, M. Gharib, and Y. Hurmuzlu, "Solving Frictionless Rocking Block Problem With Multiple Impacts," *Proceedings of the Royal Society A: Mathematical, Physical and Engineering Sciences* 465, no. 2111 (2009): 3323–3339, https://doi.org/10.1098/rspa.2009.0273.

40. M. N. Chatzis, M. García Espinosa, C. Needham, and M. S. Williams, "Energy Loss in Systems of Stacked Rocking Bodies," *Journal of Engineering Mechanics* 144, no. 7 (2018): 04018044, https://doi.org/10.1061/(ASCE)EM.1943-7889.0001443.

41. M. N. Chatzis and A. W. Smyth, "Robust Modeling of the Rocking Problem," *Journal of Engineering Mechanics* 138, no. 3 (2012): 247–262, https://doi.org/10.1061/(ASCE)EM.1943-7889.0000329.

42. E. G. Dimitrakopoulos and M. J. DeJong, "Revisiting the Rocking Block: Closed-Form Solutions and Similarity Laws," *Proceedings of the Royal Society A: Mathematical, Physical and Engineering Sciences* 468, no. 2144 (2012): 2294–2318, https://doi.org/10.1098/rspa.2012.0026.

43. Y. Zhang, R. Thiers-Moggia, and C. Málaga-Chuquitaype, "Impact and Clutch Nonlinearities in the Seismic Response of Inerto-Rocking Systems," *Bulletin of Earthquake Engineering* 21, no. 3 (2023): 1713–1745.

44. D. Kalliontzis and S. Sritharan,, "Characterizing Dynamic Decay of Motion of Free-Standing Rocking Members," *Earthquake Spectra* 34, no. 2 (2018): 843–866, https://onlinelibrary.wiley.com/doi/abs/10.1193/011217EQS013M.

45. D. Kalliontzis, S. Sritharan, and A. E. Schultz, "Improved Coefficient of Restitution Estimation for Free Rocking Members," *Journal of Structural Engineering* 142, no. 12 (2016): 06016002, https://doi.org/10.1061/(ASCE)ST.1943-541X.0001598.

46. N. Čeh, G. Jelenić, and N. Bićanić, "Analysis of Restitution in Rocking of Single Rigid Blocks," *Acta Mechanica* 229, no. 11 (2018): 4623–4642, https://doi.org/10.1007/s00707-018-2246-8.

47. C. Sandeep, K. Senetakis, D. Cheung, Y. Wang, and M. Coop, "Experimental Study on the Coefficient of Restitution of Grain Against Block Interfaces for Natural and Engineered Materials," *Canadian Geotechnical Journal* 58, no. 1 (2021): 35–48.

48. Y. Duan and Z.-G. Feng, "Incorporation of Velocity-Dependent Restitution Coefficient and Particle Surface Friction Into Kinetic Theory for Modeling Granular Flow Cooling," *Physical Review E* 96, no. 6 (2017): 062907.

49. F. Schuricht and M. Schönherr, "Divergence Theorems," in *A Theory of Traces and the Divergence Theorem* (2025), 69–161.

50. G. Marsaglia and W. W. Tsang, "The Ziggurat Method for Generating Random Variables," *Journal of Statistical Software* 5 (2000): 1–7, https://doi.org/10.18637/jss.v005.i08.

51. M. Matsumoto and T. Nishimura, "Mersenne Twister: A 623-Dimensionally Equidistributed Uniform Pseudo-Random Number Generator," *ACM Transactions on Modeling and Computer Simulation* 8, no. 1 (1998): 3–30, https://dl.acm.org/doi/10.1145/272991.272995.

52. R. Kadir and M. A. Maarof, "Randomness Analysis of Pseudorandom Bit Sequences," in *2009 International Conference on Computer Engineering and Applications* 2 (International Conference on Computer Engineering and Applications, 2011), 390–394.

53. E. Kreyszig, *Advanced Engineering Mathematics*, 10th ed. (2020).

54. M. D. Berg, O. Cheong, M. V. Kreveld, and M. Overmars, *Computational Geometry: Algorithms and Applications | Springer Nature Link*, 3rd ed. (Springer), https://link.springer.com/book/10.1007/978-3-540-77974-2.

55. A. Vaschy, "Sur les lois de similitude en physique," *Annales Telegraphiques* 19 (1892): 25–28, https://cir.nii.ac.jp/crid/1571135649100616192?lang=en.

56. E. Buckingham, "On Physically Similar Systems; Illustrations of the Use of Dimensional Equations," *Physical Review* 4, no. 4 (1914): 345–376, https://link.aps.org/doi/10.1103/PhysRev.4.345.

57. G. I. Barenblatt, *Dimensional Analysis* (Gordon and Breach Science Publishers, 1987).

58. Pacific Earthquake Engineering Research Center, "PEER NGA-West2 Ground Motion Database," Online Database (2025), accessed January 15, 2026, https://ngawest2.berkeley.edu/.

59. S. Shen and C. Málaga-Chuquitaype, "Physics-Informed Artificial Intelligence Models for the Seismic Response Prediction of Rocking Structures," *Data-Centric Engineering* 5 (2024): e1, https://www.cambridge.org/core/journals/data-centric-engineering/article/physicsinformed-artificial-intelligence-models-for-the-seismic-response-prediction-of-rocking-structures/2D0302B70454B4D14673BF1D87B8F917.

60. Y. Ishiyama, "Motions of Rigid Bodies and Criteria for Overturning by Earthquake Excitations," *Earthquake Engineering & Structural Dynamics* 10, no. 5 (1982): 635–650, https://onlinelibrary.wiley.com/doi/abs/10.1002/eqe.4290100502.

61. E. G. Dimitrakopoulos and T. S. Paraskeva, "Dimensionless Fragility Curves for Rocking Response to Near-Fault Excitations," *Earthquake Engineering & Structural Dynamics* 44, no. 12 (2015): 2015–2033, https://onlinelibrary.wiley.com/doi/abs/10.1002/eqe.2571.

62. C. Petrone, L. Di Sarno, G. Magliulo, and E. Cosenza, "Numerical Modelling and Fragility Assessment of Typical Freestanding Building Contents," *Bulletin of Earthquake Engineering* 15, no. 4 (2017): 1609–1633, https://doi.org/10.1007/s10518-016-0034-1.

63. A. I. Giouvanidis and E. G. Dimitrakopoulos, "Rocking Amplification and Strong-Motion Duration," *Earthquake Engineering & Structural Dynamics* 47, no. 10 (2018): 2094–2116, https://onlinelibrary.wiley.com/doi/abs/10.1002/eqe.3058.

64. F. Gelagoti, R. Kourkoulis, I. Anastasopoulos, and G. Gazetas, "Rocking-Isolated Frame Structures: Margins of Safety Against Toppling Collapse and Simplified Design Approach," *Soil Dynamics and Earthquake Engineering* 32, no. 1 (2012): 87–102, https://www.sciencedirect.com/science/article/pii/S0267726111002491.

65. C. Málaga-Chuquitaype, "Strong-Motion Duration and Response Scaling of Yielding and Degrading Eccentric Structures," *Earthquake Engineering & Structural Dynamics* 50, no. 2 (2021): 635–654.

66. C. A. Cornell, F. Jalayer, R. O. Hamburger, and D. A. Foutch, "Probabilistic Basis for 2000 SAC Federal Emergency Management Agency

10969845, 2026, 12, Downloaded from https://onlinelibrary.wiley.com/doi/10.1002/eqe.70244 by Imperial College London, Wiley Online Library on [12/10/2026]. See the Terms and Conditions (https://onlinelibrary.wiley.com/terms-and-conditions) on Wiley Online Library for rules of use; OA articles are governed by the applicable Creative Commons License

Steel Moment Frame Guidelines," *Journal of Structural Engineering* 128, no. 4 (2002): 526–533, https://doi.org/10.1061/(ASCE)0733-9445(2002)128:4(526).

67. E. Junda and C. Malaga-Chuquitaype, "Seismic Acceleration Demands in Tall CLT Buildings, Predictive Models and Intensity Measures," *Engineering Structures* 298 (2024): 117024.

68. S. L. Restrepo and M. C. Constantinou, "Shake Table Testing of a Seismic Isolation System for Lightweight Structures," *Earthquake Engineering & Structural Dynamics* 54, no. 2 (2025): 562–582, https://onlinelibrary.wiley.com/doi/abs/10.1002/eqe.4269.

Appendix A: Analytical Expression for the MMI

Figure A1 illustrates a regular polygon (shown here as a hexagon) inscribed in a circle. The polygon's centroid, denoted by G, coincides with the centre of the circumscribed circle. Assuming a uniform density distribution, the polygon has a total mass of $M_{polygon}$. This figure serves as the basis for deriving an expression for the MMI of the polygon about the specified axes.

Variables and Symbols:

- r_c: Radius of the circumscribed circle, defined as the distance from the centroid G to any vertex of the polygon.
- G: Centroid (mass centre) of the polygon, located at the centre of the circumscribed circle.
- O: Pivot point or axis located at one of the vertices of the polygon. The distance from G to O is equal to r_c.
- $M_{\triangle}$: Mass of one isoceles triangle, assumed to be uniformly distributed.
- $M_{polygon}$: Total mass of the polygon, assumed to be uniformly distributed.
- n: Number of sides of the regular polygon.
- s: Side length of the regular polygon, $s = 2r_c \cdot \sin(\frac{\pi}{n})$.
- I_G: MMI of the polygon about the axis passing through the centroid G and perpendicular to the plane of the polygon.
- I_O: MMI of the polygon about the parallel axis passing through the vertex O. Can be calculated using the parallel axis theorem, $I_o = I_G + M_{polygon} \cdot r_c^2$.

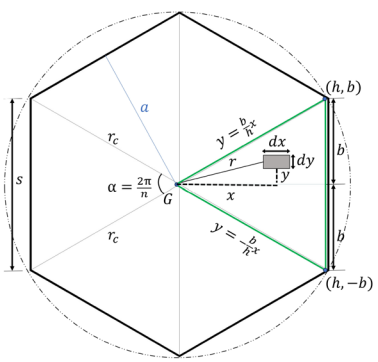


FIGURE A1 | Regular polygon with side s inscribed in a circle with radius r_c

- dx and dy: Width and height of the differential element dm, respectively.
- a: Apothem of the polygon which is equal to the height (h) of the isosceles triangle shown in green, $a = r_c \cdot \cos(\frac{\pi}{n}) = h$.
- b: Half of side length (s) which acts as the base of a right angled triangle at when apothem (a) of the polygon which is drawn, $b = \frac{s}{2} = r_c \cdot \sin(\frac{\pi}{n})$.
- A: Area of the isosceles triangle shown in green. There are n isosceles triangles in a n-sided regular polygon, $A = \frac{r_c^2}{2} \cdot \sin(\frac{2\pi}{n})$.
- α: Vertex angle subtended at the center G by two radii connecting any two consecutive vertices of the polygon, $\alpha = \frac{2\pi}{n}$.

To determine the MMI of a regular polygon with side length (s) inscribed in a circle of radius (r_c) about a pivot point O located at a polygon vertex, a uniform density distribution is assumed. The centroidal MMI, I_G, is first derived about an axis through the centroid G and perpendicular to the polygon's plane. The MMI about the parallel axis through O, denoted by I_O, is then obtained using the parallel axis theorem.

$$I_o = I_G + M_{polygon} \cdot r_c^2 \tag{A1}$$

The MMI of a planar object about an axis passing through its centroid and perpendicular to the plane is given by:

$$I_G = \int_m r^2 dm \tag{A2}$$

Equation (A2) is first applied to a single isosceles triangle. Since the polygon consists of n identical triangles, the resulting expression is multiplied by n to obtain the MMI of the entire polygon. To evaluate Equation (A2), we need to find r^2 and dm. From the geometry showing in Figure A1, we get that $r^2 = x^2 + y^2$. Furthermore, dm is the product of areal density (ρ_A) and differential area dA as displayed in Figure A1.

$$dm = \rho_A \cdot dA; \rho_A = \frac{M}{A}; dA = dxdy \tag{A3}$$

By using the Equations (A3), Equation (A2) takes the form,

$$I_{\triangle} = \int_x \int_y (x^2 + y^2)\rho_A . dydx \tag{A4}$$

To determine the limits for x and y, identical isosceles triangles. Each triangle has two equal sides of length r_c and a vertex angle of $\alpha = \frac{2\pi}{n}$. From Figure A1, the line from centre to vertex (h, b) is $y = \frac{b}{h}x$ and the line from centre to other vertex $(h, -b)$ is $y = -\frac{b}{h}x$.

The limits of integration depend on the shape of the triangle: (1) For x: From 0 to h; and (2) For y: From $-\frac{b}{h}x$ to $\frac{b}{h}x$.

So, the integral becomes:

$$I_{\triangle} = \rho_A \int_{x=0}^{h} \int_{y=-\frac{b}{h}x}^{\frac{b}{h}x} (x^2 + y^2) dydx \tag{A5}$$

Evaluating the double integral yields the MMI of a single triangle $I_{\triangle}$. To get the MMI of the polygon (I_G) about the mass centre of the n-sided polygon, answer of Equation (A5) would be multiplied with n.

$$I_{\triangle} = \rho_A \left(\frac{bh^3}{2} + \frac{b^3 h}{6} \right) \tag{A6}$$

The total mass ($M_{\triangle}$) of the triangle is: $M_{\triangle} = \rho_A \cdot$ Area of isosceles triangle. Its area: $A = \frac{1}{2} \cdot \text{base} \cdot \text{height} = \frac{1}{2} \cdot 2b \cdot h =$

10969845, 2026, 12, Downloaded from https://onlinelibrary.wiley.com/doi/10.1002/eqe.70244 by Imperial College London, Wiley Online Library on [12/10/2026]. See the Terms and Conditions (https://onlinelibrary.wiley.com/terms-and-conditions) on Wiley Online Library for rules of use; OA articles are governed by the applicable Creative Commons License

bh; $M_{\triangle} = \rho_A \cdot bh$. Substituting $\rho_A = \frac{M_{\triangle}}{bh}$ into the MMI Equation (A6): $I_{\triangle} = M_{\triangle}\left(\frac{h^2}{2} + \frac{b^2}{6}\right)$ Substituting h and b, Equation (A6) becomes:

$$I_{\triangle} = M_{\triangle} \cdot r_c^2 \left(\frac{1 + 2\cos^2\left(\frac{\pi}{n}\right)}{6} \right) \tag{A7}$$

Equation (A7) is MMI for one isosceles triangle.

MMI of one n-sided regular polygon about an axis that passes through the centroid/mass center which is perpendicular to the plane is obtained after multiplying Equation (A7) with n, we get:

$$I_G = n \times \left[M_{\triangle} \cdot r_c^2 \left(\frac{1 + 2\cos^2\left(\frac{\pi}{n}\right)}{6} \right) \right] \tag{A8}$$

Substituting I_G from Equation (A8) to Equation (A1), we get the required expression for MMI about any vertex of a regular polygon.

$$I_o = n \times M_{\triangle} \cdot r_c^2 \left(\frac{1 + 2\cos^2\left(\frac{\pi}{n}\right)}{6} \right) + M_{polygon} \cdot r_c^2 \tag{A9}$$

Based on geometry, we can derive that $M_{\triangle} = \frac{M_{polygon}}{n}$ and substituting in above equation and simplifying:

$$I_o = r_c^2 \cdot M_{polygon} \left[\frac{7 + 2\cos^2\left(\frac{\pi}{n}\right)}{6} \right] \tag{A10}$$

In the limit, as $n \to \infty$ the polygon approaches a circular shape and Equation (A10) converges to $I_o = \frac{2}{3} M_{polygon} r_c^2$, which corresponds to the moment of inertia of a rigid disc about a point support.

10969845, 2026, 12, Downloaded from https://onlinelibrary.wiley.com/doi/10.1002/eqe.70244 by Imperial College London, Wiley Online Library on [12/10/2026]. See the Terms and Conditions (https://onlinelibrary.wiley.com/terms-and-conditions) on Wiley Online Library for rules of use; OA articles are governed by the applicable Creative Commons License